Control-volume method for numerical simulation of two-phase immiscible flow in two- and three-dimensional discrete-fractured media

J. E. P. Monteagudo and A. Firoozabadi

Reservoir Engineering Research Institute, Palo Alto, California, USA

[1]   We provide a numerical procedure for the simulation of two-phase immiscible and incompressible flow in two- and three-dimensional discrete-fractured media. The concept of cross-flow equilibrium is used to reduce the fracture dimension from n to $(n-1)$ in the calculation of flow in the fractures. This concept, which is often referred to as the discrete-fracture model, has a significant effect on the reduction of computational time. The spatial discretization is performed with the control-volume method. This method is locally conservative and allows the use of unstructured grids to represent complex geometries, such as discrete-fracture configurations. The relative permeability is upwinded with a criterion based on the evaluation of the flux direction at the boundaries of the control volumes, which is consistent with the physics of fluid flow. The system of partial differential equations is decoupled and solved using the implicit-pressure, explicit-saturation (IMPES) approach. The algorithm has been successfully tested in two- and three-dimensional numerical simulations of wetting phase fluid injection (such as water) in discrete-fractured media saturated by a nonwetting phase (such as nonaqueous phase liquid or oil) with mild to high nonlinearity in relative permeability and capillary pressure. To the best of our knowledge, results for simulations of two-phase immiscible and incompressible flow in three-dimensional discrete-fractured media, including capillary and gravity effects, are the first to appear in the literature.   *INDEX TERMS:* 1829 Hydrology: Groundwater hydrology; 3210 Mathematical Geophysics: Modeling; 3230 Mathematical Geophysics: Numerical solutions; 3299 Mathematical Geophysics: General or miscellaneous; *KEYWORDS:* two-phase three-dimensional flow, control volume simulation, discrete-fractured media

Citation: Monteagudo, J. E. P., and A. Firoozabadi (2004), Control-volume method for numerical simulation of two-phase immiscible flow in two- and three-dimensional discrete-fractured media, *Water Resour. Res.*, *40*, W07405, doi:10.1029/2003WR002996.

1.   Introduction

[2]   There is wide interest in the numerical simulation of multiphase flow in fractured-porous media where, unlike single-phase flow, high-permeability fractures may not be the main conduit to flow of different phases [*Firoozabadi and Ishimoto*, 1994]. Multiphase flow in subsurface fractured-hydrocarbon formations is of high interest in hydrocarbon production. Flow in fractured-geothermal reservoirs and underground storage of fluids are also of interest to the energy production industry. The study of the flow of water and the non-aqueous-phase liquids (NAPLs) in fractured media is another example. The main motivation of our work relates to fractured-hydrocarbon formations which provide around 20 percent of world oil and gas production.

[3]   Fractured-porous media are composed of rock matrix and fractures. Depending on the geophysical formation, fractures may be represented by connected orthogonal fractures or by discrete fractures. The former is known as the sugar-cube representation. Often the rock matrix provides the storage, and in single-phase flow, fractures provide the fluid flow path. In two-phase flow, fractures may provide the flow path of one phase and the less permeable matrix can provide the flow path of the other phase [*Tan and Firoozabadi*, 1995]. The flow path of a phase in multiphase flow is affected by capillary, gravity, diffusion/dispersion, and viscous forces.

[4]   In some fractured-porous media, the fluids are nearly equally distributed in rock matrix and fractures. There are also geological formations in which there is very little porosity in the rock matrix; all the fluids are stored in the fractures.

[5]   Numerical simulation of multiphase flow in two-dimensional (2-D) and 3-D connected (sugar-cube representation) and especially discrete-fractured media is a challenging task. The large contrast in rock matrix and fracture permeability and small fracture aperture (often of the order of 0.1 mm or less in subsurface reservoirs) make the problem of numerical simulation very complicated with most numerical schemes. The nonlinearity from capillary pressure and relative permeability can also complicate the numerical simulation.

[6]   In the past, dual-porosity/dual-permeability models [*Warren and Root*, 1963; *Kazemi*, 1969; *Thomas et al.*, 1983] have been used for simulation of multiphase flow in

2-D and 3-D fractured media for hydrocarbon-recovery processes. These models are, however, limited to sugar-cube representation of fractured media. Another main drawback of dual-porosity/dual-permeability models is that one has to provide the fluid-flow exchange term between the fracture and matrix. The exchange term may not be properly described with gravity and viscous effects. Because the dual-porosity/dual-permeability models have been incorporated in finite difference discretization schemes, the numerical dispersion is also of concern for certain applications. Several well-known commercial and noncommercial packages use the dual-porosity or dual-porosity/dual-permeability models. Among them are TOUGH2 [*Pruess et al.*, 1999], STAR [*Pritchett*, 1995], ECLIPSE-2000A (from Schlumberger-Geoquest, 2000), and FEHM [*Zyvoloski et al.*, 1994]. From these packages, only TOUGH2 and FEHM are intended for unstructured grids. Despite widespread use of these software for a broad range of applications, they cannot be used for the numerical simulation of immiscible two-phase flow in a fractured porous medium with discrete fractures in 2-D and especially in 3-D.

[7] An alternative to dual-porosity/dual-permeability models is the discrete-fracture model [*Noorishad and Mehran*, 1982; *Baca et al.*, 1984; *Granet et al.*, 1998]. The discrete-fracture model is based on the concept of cross-flow equilibrium between the fluids in the fractured node and the matrix node next to the fracture. (Note that the discrete-fracture model has no relation to the discrete fracture configuration. The model can be used for a sugar-cube representation of fractures as well as discrete fractures.) In the discrete-fracture model the dimensionality of fractures is reduced from n to (n-1). This reduction greatly decreases the computational time. When compared with the dual-porosity/dual-permeability models, the discrete-fracture model offers several advantages: It can account explicitly for the effect of individual fractures on fluid flow; there is no need to compute the exchange term between the matrix and the fracture; and the performance of the method is not affected by very thin fractures. It also reduces computational time by orders of magnitude in 2-D and 3-D as pointed out earlier. Despite all these advantages, there is no loss of accuracy when the results from the discrete fracture model are compared with the full n-dimensional fracture flow [*Karimi-Fard and Firoozabadi*, 2003]. The discrete-fracture model has been employed by several authors to develop codes for multiphase flow in fractured porous media [*Kim and Deo*, 1999, 2000; *Bastian et al.*, 2000; *Karimi-Fard and Firoozabadi*, 2003; *Karimi-Fard et al.*, 2003; *Geiger et al.*, 2003].

[8] The discrete-fracture model poses a challenge for the discretization of the domain through a proper mesh. Typically, numerical-reservoir simulation is dominated by fast finite difference codes with structured meshes for representation of reservoir domain. Structured meshes are not suited for the representation of complex geometries such as discrete-fractured media. The discrete-fracture representation requires a conforming unstructured mesh, where the (n-1) dimensional fracture elements share nodes and faces with the corresponding n-dimensional matrix elements at the matrix-fracture interface. In addition, high-quality mesh elements are required to satisfy certain geometrical constraints, such as dihedral angles and aspect ratio; otherwise

the conditioning of the spatial discretization matrix may be affected, resulting in the numerical instability of the flow computation [*Fleischmann et al.*, 1999]. While in 2-D, a conforming Delaunay triangulation suffices to obtain a high-quality mesh, the same is not true in 3-D, where the generation of high-quality tetrahedra conforming to an embedded surface is still an open problem. Several methods to improve the quality of a 3-D unstructured Delaunay mesh have been recently developed [*Freitag and Ollivier-Gooch*, 1996], but they may not apply to a tetrahedrization conforming to an embedded 2-D surface since the improvement is generally based on vertex displacements and edge swappings, changes which may not be applicable at the matrix-fracture interface. The above restrictions must be taken into account when implementing numerical methods for the simulation of multiphase flow in 3-D unstructured meshes.

[9] Multiphase flow in fractured media can be classified as miscible, partial mixing of phases and immiscible problems depending on miscibility between the phases. In this work the immiscible problem in two-phase state will be addressed. We also make the further assumption of incompressible and isothermal flow. Two-phase incompressible flow may be modeled with two partial differential equations: the flow potential and the saturation equation. The former is elliptic and the latter is of the convection-diffusion type, degenerating to hyperbolic type when the capillary pressure is neglected. There are several possible formulations based on the choice of the wetting or nonwetting phase variables. The formulation used in our work will be detailed later.

[10] Several numerical methods have been employed in the past for the simulation of 2-D multiphase flow in porous media, such as the classical finite element method (C-FEM), the streamline-upstream Petrov-Galerkin finite element method (SUPG-FEM), the fully upwind finite element method (FU-FEM), and the control-volume method (CV). *Helmig* [1997] provides a detailed review of these methods.

[11] The C-FEM and SUPG-FEM are inadequate for the purpose of numerical simulation of immiscible displacement in discrete-fractured media. It is widely known that because of the inherent instability for the first-order derivatives in space, the C-FEM is not suitable for mild to the highly nonlinear convective-dominated immiscible displacement problems [*Lewis et al.*, 1974; *Lemmonier*, 1979; *Rabbani and Warner*, 1994]. The SUPG-FEM [*Brooks and Hughes*, 1982; *Hughes and Mallet*, 1986] overcomes the instability of the C-FEM, but recent works have shown that this method can produce unphysical results when used for the simulation of two-phase flow in highly contrasted heterogeneous porous media [*Helmig*, 1997; *Helmig and Huber*, 1998].

[12] The FU-FEM, first proposed by *Dalen* [1979], gives a physically correct result for two-phase immiscible flow in 2-D porous media [*Dalen*, 1979; *Huyakorn et al.*, 1983; *Rabbani*, 1994; *Helmig and Huber*, 1998]. (An analysis of the FU-FEM is given by *Helmig* [1997].) In this method the computation of the FEM stiffness matrix in 2-D Delaunay mesh is modified by assembling a node-balance flow system of equations. In addition, the wetting phase mobility at the triangle edges is upwinded according to the difference between wetting phase potentials at the edge nodes.

[13] The FU-FEM has been recently employed for 2-D numerical simulation of two-phase immiscible flow in the context of discrete-fractured media [*Kim and Deo*, 1999, 2000; *Karimi-Fard and Firoozabadi*, 2003]. However, *Kim and Deo* [1999] reported the failure of the method when extended to 3-D problems. The authors concluded that the stability was mesh-dependent. In fact, as will be discussed later, the problem is caused by the upwind criterion of *Dalen* [1979], which produces unphysical saturations for 3-D Delaunay meshes. Instead, *Forsyth* [1991] used the direction of a single-phase flow between edge nodes as the upwinding criterion: The flow potential difference between edge nodes is multiplied by a single-phase transmissibility term, which may be negative in 3-D Delaunay meshes. To reduce negative transmissibilites, *Letniowski and Forsyth* [1991] proposed a tetrahedral mesh generation based on the decomposition of a regular grid. However, this proposal is not appropriate for the unstructured conforming mesh generation in the discrete-fracture approach.

[14] For the sake of clarity, we would like to make a remark regarding proliferation of terms in the literature, related to the control-volume method. Some authors [*Forsyth*, 1990, 1991; *Letniowski and Forsyth*, 1991; *Helmig*, 1997] refer to the FU-FEM as the control-volume finite element method and to the CV method as the control-volume box method.

[15] The CV method was first proposed in the computational fluid dynamics by *Baliga and Patankar* [1980]. The method is in essence a finite volume formulation over dual cells (control volumes) of a Delaunay mesh, which makes the CV method have distinct advantages over the FU-FEM: (1) It is locally conservative; (2) the upwind criterion is based on the analysis of the flow direction at the boundaries of the control volumes, which has a clear physical interpretation; and (3) it can include finite volume concepts for hyperbolic and convection-diffusion partial differential equations such as numerical fluxes and high-order upwinding [*Barth and Jespersen*, 1989].

[16] Because of these features, the CV method has been used mainly to solve the saturation equation of the two-phase immiscible flow in porous media [*Verma*, 1996; *Helmig*, 1997]. The convergence of the CV numerical method for two-phase immiscible flow in porous media has been recently proved by *Michel* [2003]. Perhaps the only drawback of the method is the requirement of generating a dual mesh, but this does not affect the algorithm performance for a fixed mesh.

[17] *Bastian et al.* [2000] and *Geiger et al.* [2003] have employed the CV method for the numerical simulation of two-phase flow in 2-D fractured media. *Bastian et al.* [2000] developed the MUFTE-UG simulator that uses the discrete-fracture model and present a 2-D example for gas infiltration into fractured media composed of five discrete fractures with a thickness of 4 cm (very thick fractures). The fracture and matrix capillary pressures functions were similar. *Bastian et al.* [2000] also included gravity in their work. *Geiger et al.* [2003] use the C-FEM for the solution to the flow potential and the CV method for the saturation equation. These authors did not use the concept of cross-flow equilibrium, and therefore the computational speed

for fractured media may be very low. They also neglected capillary pressure, despite its significance in immiscible fluid flow in fractured porous media [*Terez and Firoozabadi*, 1999; *Karimi-Fard and Firoozabadi*, 2003].

[18] This paper is structured along the following lines. In section 2 we present a mathematical formulation for two-phase incompressible flow in fractured media, clearly establishing physically based relations between matrix and fracture variables. This formulation has not been presented in the previous related works [*Kim and Deo*, 1999, 2000; *Bastian et al.*, 2000; *Karimi-Fard and Firoozabadi*, 2003; *Geiger et al.*, 2003]. In section 3 we provide an efficient procedure to numerically solve the two-phase flow equations in fractured media using the discrete-fracture model within the framework of the CV method. We solve both the wetting phase flow potential and saturation equations with the CV method in 2-D and 3-D and provide a detailed description on how to incorporate fractures and matrix in the numerical scheme with the CV method. The 3-D formulation for fractured porous media is new. We also analyze the influence of different upwind criteria on the robustnesses of the FU-FEM and CV method. In section 4 our proposed method is thoroughly tested with several numerical examples, where varying degrees of nonlinearity in relative permeability and capillary pressure are considered. To the best of our knowledge, this is the first time that 3-D simulation for the discrete-fracture model with capillary pressure and gravity effects are modeled numerically. We provide concluding remarks in section 5.

2. Governing Equations

2.1. Two-Phase Incompressible Flow in Porous Media

[19] The standard equations describing two-phase incompressible, immiscible flow displacement in porous media are the balance equations for each phase:

$$\frac{\partial \phi S_n}{\partial \tau} - \nabla \cdot \left(\frac{k_{rn} \mathbf{k}}{\mu_n} (\nabla p_n + \rho_n g \nabla z) \right) - q_n = 0 \qquad (1)$$

$$\frac{\partial \phi S_w}{\partial \tau} - \nabla \cdot \left(\frac{k_{rw} \mathbf{k}}{\mu_w} (\nabla p_w + \rho_w g \nabla z) \right) - q_w = 0 \qquad (2)$$

and the following relations:

$$S_n + S_w = 1 \qquad (3)$$

$$p_n - p_w = P_c(S_w), \qquad (4)$$

where the subscripts n and w refer to the nonwetting and wetting phase, respectively; p_i, S_i, k_{ri}, μ_i, ρ_i, and q_i are the pressure, saturation, relative permeability, viscosity, density, and source/sink term, each with respect to phase i; $\mathbf{k}$ is the absolute permeability tensor, ϕ is the porosity, P_c is the capillary pressure, g is the acceleration of gravity, z is the vertical coordinate (positive in the upward direction); and τ denotes the time. In this work we consider an isotropic medium, and thus the permeability tensor is reduced to the scalar k.

[20] To simplify the above expressions we define the mobility of phase i, λ_i, by

$$\lambda_i = \frac{k_{ri}k}{\mu_i} \qquad (5)$$

and the flow potential of phase i, Φ_i, defined by

$$\Phi_i = p_i + \rho_i gz, \qquad (6)$$

which are commonly employed in formulations of two-phase flow in porous media [Aziz and Settari, 1979]. In addition, we define the capillary flow potential, Φ_c, by

$$\Phi_c = \Phi_n - \Phi_w = P_c + (\rho_n - \rho_w)gz. \qquad (7)$$

[21] The notion of capillary pressure potential is first introduced in the work of Karimi-Fard and Firoozabadi [2003]. Next, we add equations (1) and (2), keeping the wetting phase conservation equation (2) and use relations (3) and (4) to express the remaining equations in terms of Φ_w and S_w. With this procedure, the system of equations (1)–(4) is reduced to two partial differential equations:

$$-\nabla \cdot ((\lambda_n + \lambda_w)\nabla\Phi_w) - \nabla \cdot (\lambda_n \nabla\Phi_c) - (q_n + q_w) = 0 \qquad (8)$$

$$\frac{\partial(\phi S_w)}{\partial\tau} - \nabla \cdot (\lambda_w(\nabla\Phi_w)) - q_w = 0. \qquad (9)$$

Equation (8) is referred to as the flow potential equation, which is elliptic in nature, while equation (9) is referred to as the saturation equation, which can be seen as a convection-diffusion equation [Peaceman, 1977].

[22] The boundary conditions are assumed to be impervious:

$$\mathbf{v}_w \equiv -\lambda_w \nabla\Phi_w = 0 \qquad (10)$$

$$\mathbf{v}_n \equiv -\lambda_n \nabla\Phi_n = 0, \qquad (11)$$

where $\mathbf{v}_i$ is the velocity of phase i. We must point out that the model is not restricted to the above boundary conditions. Other boundary conditions can be readily established and wells can be considered in the matrix and in the fracture using source/sink terms. Indeed we have performed simulations for large-scale problems including Dirichlet and impervious boundary conditions and producing wells in the fractures. Results will appear in a future publication.

2.2. Discrete-Fracture Model

[23] In the discrete-fracture model, the system of equations (8) and (9) is integrated by using the superposition principle. For example, for a 2-D matrix with 1-D embedded fractures, the total domain Ω can be decomposed into

$$\Omega = \Omega_m + \varepsilon\Omega_f, \qquad (12)$$

where Ω_m and $\varepsilon\Omega_f$ represent the matrix and the fracture subdomains, respectively, and ε denotes the thickness of the 1-D fracture.

[24] Equations (8) and (9) apply to both the matrix and the fracture flow. Therefore the integration of equations (8) and (9) can be written as

$$\int_\Omega \mathbf{f}\, d\Omega = \int_{\Omega_m} \mathbf{f}^m d\Omega_m + \varepsilon \int_{\Omega_f} \mathbf{f}^f d\Omega_f = 0, \qquad (13)$$

where $\mathbf{f}$ represents the residual of the system of equations (8) and (9) and superscripts m and f denote the matrix and fracture subdomains, respectively. After linearizing the nonlinear terms and discretizing in space and time, we obtain a system of linear equations:

$$\int_\Omega \mathbf{f}\, d\Omega = \mathbf{A}^m \mathbf{x}^m - \mathbf{b}^m + \mathbf{A}^f \mathbf{x}^f - \mathbf{b}^f = 0, \qquad (14)$$

where

$$\mathbf{x} = [\Phi_w,\ S_w]^T. \qquad (15)$$

[25] In the past, equation (14) has been solved as

$$(\mathbf{A}^m + \mathbf{A}^f)\mathbf{x} - \mathbf{b}^m - \mathbf{b}^f = 0 \qquad (16)$$

[Kim and Deo, 1999, 2000; Karimi-Fard and Firoozabadi, 2003], implying that $\mathbf{x}^m = \mathbf{x}^f = \mathbf{x}$, which is true only for some specific cases, as we will see later. Equation (16) lacks a relationship between the matrix and fracture variables based on physical grounds. Below, we provide a formulation for a 2-D matrix/1-D fracture flow with a coherent relationship between the matrix and fracture variables at the matrix-fracture interface. The formulation can be readily extended to 3-D matrix/2-D fracture configurations.

[26] The system of equations for the 2-D matrix domain is

$$-\nabla \cdot \left((\lambda_n^m + \lambda_w^m)\nabla\Phi_w^m\right) - \nabla \cdot \left(\lambda_n^m \nabla\Phi_c^m\right) - \left(q_n^m + q_w^m\right) = 0 \quad (17)$$

$$\frac{\partial\left(\phi^m S_w^m\right)}{\partial\tau} - \nabla \cdot \left(\lambda_w^m \left(\nabla\Phi_w^m\right)\right) - q_w^m = 0 \qquad (18)$$

and for the 1-D fracture domain is

$$-\frac{\partial}{\partial\xi}\left((\lambda_n^f + \lambda_w^f)\frac{\partial\Phi_w^f}{\partial\xi}\right) - \frac{\partial}{\partial\xi}\left(\lambda_n^f\left(\frac{\partial\Phi_c^f}{\partial\xi}\right)\right) \\ - (q_w^f + q_n^f) = 0 \qquad (19)$$

$$\frac{\partial(\phi^f S_w^f)}{\partial\tau} - \frac{\partial}{\partial\xi}\left(\lambda_w^f\left(\frac{\partial\Phi_w^f}{\partial\xi}\right)\right) - q_w^f = 0, \qquad (20)$$

where ξ is the coordinate along the fracture direction.

[27] The closure relationships between fracture and matrix variables are based on the assumption of the equality of the flow potentials, that is, $\Phi_i^m = \Phi_i^f$, where $i = \{w, n\}$. This implies that the capillary potential must be equal also:

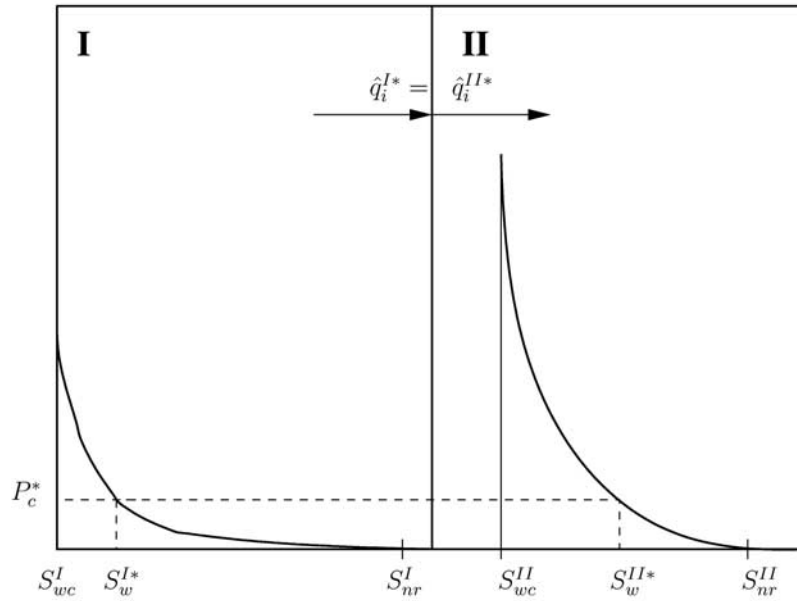$$\Phi_c^m(S_w^m) = \Phi_c^f(S_w^f). \qquad (21)$$

Figure 1. Capillary pressure and flux continuity at the interface of two media: fracture (I) and matrix (II) (asterisk denotes values at interface; $i = w, n$).

[28] Since at any given point of the matrix-fracture interface the vertical coordinate is the same, equation (21) reveals that the matrix and fracture capillary pressure should be the same at the matrix-fracture interface. This analysis is equivalent to the capillary continuity concept of *Firoozabadi and Hauge* [1990] for fractured media and similar to the one provided by *van Duijn et al.* [1994] for heterogeneous porous media. A more general approach is the use of the cross-flow equilibrium concept to derive equation (21), which will be presented in Appendix A. For displacement of a nonwetting phase by a wetting phase, there is no threshold capillary pressure. Figure 1 illustrates the concept of capillary and flux continuity at the interface of two different media, I and II. At the interface both media have the same capillary pressure $P_c^I = P_c^{II} = P_c^*$, and depending on the matrix and fracture capillary pressure functions, water saturations S_w^{I*} and S_w^{II*} may be discontinuous at the interface. Also, there is continuity of fluxes of both phases across the interface $\hat{q}_i^{I*} = \hat{q}_i^{II*}$, where $i = w, n$. We remark that since we are integrating the flow equations using the superposition principle, these terms cancel when we add the fracture and matrix flow equations. That is the reason that we omit the fluxes at the interface of the matrix and the fractures in our flow equations. For the purpose of clarity, Appendix A provides the details. Employing the capillary pressure continuity condition there evolves a clear physical relationship between S_w^m and S_w^f at the matrix-fracture interface:

$$S_w^f = \left[P_c^f\right]^{-1} P_c^m\left(S_w^m\right). \qquad (22)$$

[29] Equation (20) can be expressed in terms of S_w^m by using equation (22) and applying the chain rule:

$$\frac{dS_w^f}{dS_w^m} \frac{\partial\left(\phi^f S_w^m\right)}{\partial\tau} - \frac{\partial}{\partial\xi}\left(\chi_w^f\left(\frac{\partial\Phi_w^f}{\partial\xi}\right)\right) - q_w^f = 0. \qquad (23)$$

[30] Therefore the assumption made by *Kim and Deo* [1999, 2000] and *Karimi-Fard and Firoozabadi* [2003] that $\mathbf{x}^m = \mathbf{x}^f = \mathbf{x}$ in equation (16) is only valid if $dS_w^f/dS_w^m = 1$ along the whole saturation domain $S_{wc} \le S_w \le (1 - S_{nr})$ for each phase. In other words, when the capillary pressure functions in the fracture and the matrix are the same, then $dS_w^f/dS_w^m = 1$. With different matrix and fracture capillary pressure expressions one needs to compute the relevant dS_w^f/dS_w^m. We remark that the soure/sink term q_w^f in equation (23) allows the possibility of a well in the fracture. There is no need to compute an exchange term between the matrix and fracture since these terms will cancel when the matrix and flow equations are added in the control volume cell as stated above (see Appendix A).

3. Numerical Method

[31] In this section we define the median dual of 2-D and 3-D Delaunay meshes. Then we detail the CV spatial discretization within the discrete-fracture model. We also compare the upwinding criteria used in the CV method and the FU-FEM and provide the IMPES formulation for the discretized equations.

3.1. Two- and Three- Dimensional Delaunay-Median Dual Mesh for Discrete-Fractured Media

[32] Figure 2 shows an extract of a 2-D Delaunay triangulation of a 2-D matrix/1-D fracture configuration, where the thick line represents a fracture. The Delaunay triangulation shown in this figure is conforming to the 1-D fracture. The thick line is divided into several segments that are edges of the Delaunay triangles surrounding the 1-D fracture. Analogous discretization can be carried in a 3-D matrix/2-D fracture configuration, where the 2-D embedded surface is decomposed in triangular elements that are faces of the tetrahedra surrounding the matrix-fracture interface.
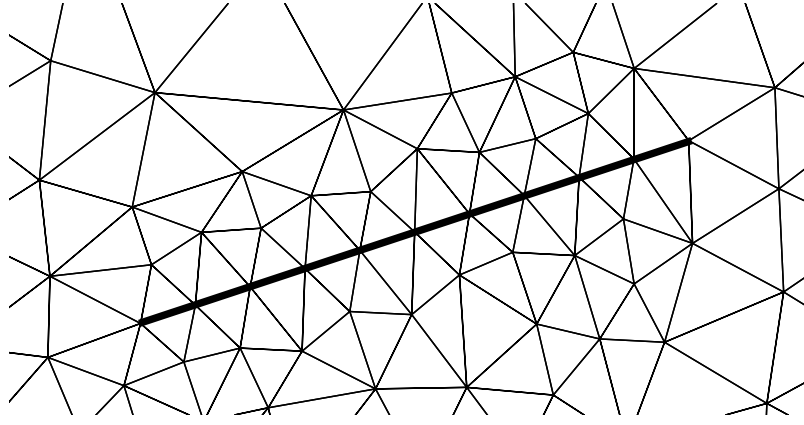
Figure 2. Extract of two-dimensional (2-D) Delaunay triangulation conforming to a 1-D fracture (thick line).

[33] In a 2-D or 3-D Delaunay mesh, each triangle or tetrahedron edge links two neighboring CV cells with the same flux across the shared interface. Therefore, from the performance standpoint, it is advantageous to use an edge-based data structure. To define a 2-D or 3-D CV cell within such a data structure, we introduce the following notation:

$\mathfrak{T}^n$ Delaunay mesh in an n-dimensional domain Ω_n with boundary Γ_n, where $n = 2$ or 3;

$\mathcal{I}$ set of vertices in $\mathfrak{T}^n$;

$\mathcal{N}_i$ set of i neighboring vertices, $\forall i \in I$;

M_{ij} midpoint of the edge $\overline{ij}$ connecting the neighboring nodes $i, j \in \mathcal{I}$;

$\mathcal{T}_{ij}$ set of elements t (triangles in 2-D Delaunay mesh or tetrahedra in 3-D Delaunay mesh) sharing the edge $\overline{ij}$;

G_t barycenter of element $t \in \mathcal{T}_{ij}$.

For the tetrahedra in a 3-D Delaunay mesh, we require the additional definitions:

$\mathcal{F}_{ij}^t$ set of triangular faces, $\{f_{ij,1}^t, f_{ij,2}^t\}$, of tetrahedron $t \in \mathcal{T}_{ij}$ sharing the edge $\overline{ij}$;

$C_{ij,k}^t$ barycenter of the triangular face $f_{ij,k}^t \in \mathcal{F}_{ij}^t$.

[34] The 2-D median-dual cell, V_i^2, in $\mathfrak{T}^2$ around an arbitrary node $i \in \mathcal{I}$ is a polygon with the boundary defined by

$$\Gamma_{V_i^2} = \bigcup_{j \in \mathcal{N}_i} \bigcup_{t \in \mathcal{T}_{ij}} \overline{G_t M_{ij}}. \tag{24}$$

[35] The measure and outward normal of each segment $\overline{G_t M_{ij}}$ are denoted by e_{jt} and $\mathbf{n}_{jt}$, respectively. In Figure 3 we show an example of a 2-D CV cell including a fracture edge. In all the 2-D numerical examples, the 2-D Delaunay triangulation conforming to the 1-D fracture elements were generated with the package triangle [*Shewchuk*, 1996], a public domain software available at www-2.cs.cmu.edu/~quake/triangle.html.

[36] The 3-D median-dual cell, V_i^3, in $\mathfrak{T}^3$ around an arbitrary node $i \in \mathcal{I}$ is a polyhedron with boundary

$$\Gamma_{V_i^3} = \bigcup_{j \in \mathcal{N}_i} \bigcup_{t \in \mathcal{T}_{ij}} \overline{G_t C_{ij,1}^t M_{ij} C_{ij,2}^t}. \tag{25}$$

[37] We denote by $a_{t,ij}$ and $\boldsymbol{\sigma}_{t,ij}$ the measure and outward normal of each quadrilateral $\overline{G_t C_{ij,1}^t M_{ij} C_{ij,2}^t}$ forming $\Gamma_{V_i^3}$. In Figure 4 we show an example of a tetrahedra of $\mathfrak{T}_3$ at the 3-D matrix/2-D fracture interface.

[38] For the 3-D numerical examples, we tested three public domain tetrahedral mesh generators to perform a Delaunay tetrahedrization conforming to the fractures: GRUMMP, developed by Oliver-Gooch and available at http://tetra.mech.ubc.ca/GRUMMP; gmsh, developed by Geuzaine and Remacle, available at http://www.geuz.org/gmsh; and tetgen [*Si*, 2002], available at http://tetgen.
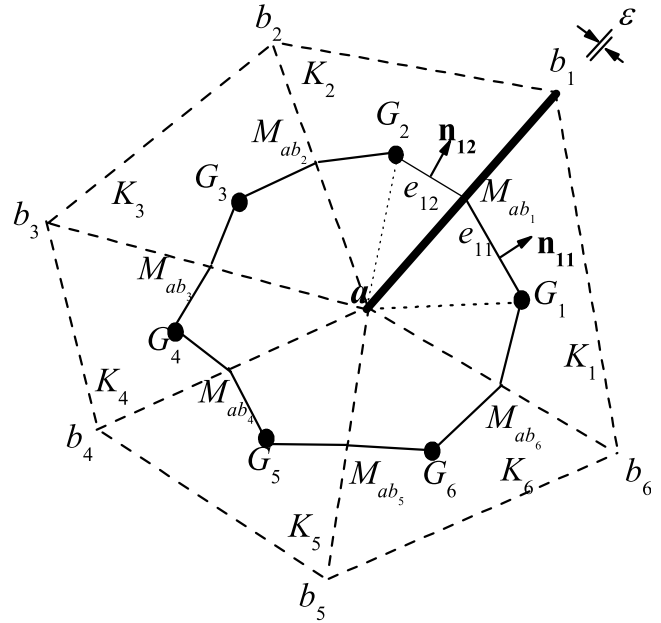

Figure 3. A 2-D CV cell (thin solid lines) formed from the median-dual of a 2-D Delaunay triangulation (dashed lines). The node a is surrounded by the set of nodes $\mathcal{N}_a = \{b_1, b_2 \ldots b_6\}$. The fracture edge $\overline{ab_1}$ (thick solid line) with midpoint M_{ab_1} is shared by two triangles $\mathcal{T}_{ab_1} = \{K_1, K_2\}$ with barycenters G_1 and G_2, respectively. The segments $\overline{G_1 M_{ab_1}}$ and $\overline{G_2 M_{ab_1}}$ with outward normals $\mathbf{n}_{11}$ and $\mathbf{n}_{12}$, respectively, are part of the boundary of the 2-D CV cell around node a.
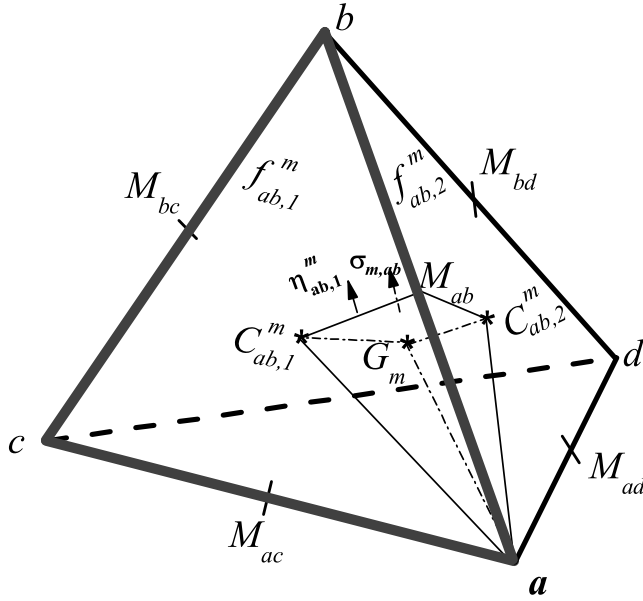
Figure 4. Section of a 3-D CV cell in a tetrahedron $m \in \mathcal{T}_{ab}$, with barycenter G_m. Edge $\overline{ab}$ is shared by faces $f^m_{ab,1}$ and $f^m_{ab,2}$ with barycenters $C^m_{ab,1}$ and $C^m_{ab,2}$, respectively. Face $f^m_{ab,1}$, shown in thick lines, is shared by the 3-D matrix and the 2-D fracture. The quadrilateral $\overline{G_m C^m_{ab,1} M_{ab} C^m_{ab,2}}$, with outward normal $\boldsymbol{\sigma}_{m,ab}$, is part of the boundary of the 3-D CV cell around node a. In the fracture face, $f^m_{ab,1}$, the segment $\overline{C^m_{ab,1} M_{ab}}$, with outward normal $\boldsymbol{\eta}^m_{ab,1}$ is part of the boundary of a 2-D CV cell (in the coordinates of the fracture plane) around node a.

berlios.de. Only tetgen produced good quality tetrahedrization conforming to the 2-D fractures contained in the domain. However, depending on the number of fractures, angle of incidence of the fractures, or degree of refinement, tetgen may not produce good quality meshes or may even fail.

3.2. Variables and Gradient Approximation

[39] Saturation variables (S_w, S_n) are considered constant inside each CV cell, and flow potential variables (Φ_w, Φ_n, Φ_c) are approximated inside each Dealunay-mesh element (triangle or tetrahedron) by linear approximations:

$$\Psi(\mathbf{x}) = \sum_{i=1}^{nv} N_i(\mathbf{x}) \Psi_i, \qquad (26)$$

where nv is the number of vertices of the element, Ψ_i represents any flow potential variable at nodes i with coordinates $\mathbf{x}_i$, and N_i is the shape function defined by

$$N_i(\mathbf{x}) = \frac{\alpha_i + \beta_i x + \gamma_i y}{2A} \qquad (27)$$

for triangles and by

$$N_i(\mathbf{x}) = \frac{\alpha_i + \beta_i x + \gamma_i y + \delta_i z}{6V} \qquad (28)$$

for tetrahedra.

[40] In equation (27), A is the area of the triangular element, and in equation (28), V represents the volume of the tetrahedral element. Details on the computation of the coefficients α_i, β_i, γ_i, and δ_i for triangular and tetrahedral elements are described by *Zienkiewicz and Taylor* [2000]. From equation (26), the gradient of any variable inside a triangular or tetrahedral element is constant:

$$\nabla \Psi = \sum_{i=1}^{nv} \Psi_i \nabla N_i(\mathbf{x}), \qquad (29)$$

where $\mathbf{x}$ represents coordinates in the corresponding element dimension.

3.3. Spatial Discretization

[41] In our work, both the flow potential and saturation equations (equations (8) and (9)) are solved in the CV-dual cells of a 2-D and 3-D Delaunay mesh.

[42] We will illustrate the methodology of the CV spatial discretization in the discrete-fracture framework by solving the saturation equation (equation (9)) for a 2-D matrix/1-D fracture system. The same methodology can be applied to the flow potential equation (equation (8)).

[43] Integrating equation (9) in a control volume $V_i^2 \in \mathfrak{T}^2$:

$$\int_{V_i^2} \phi \frac{\partial S_w}{\partial \tau} dA - \int_{V_i^2} \nabla \cdot (\lambda_w \nabla \Phi_w) dA - \int_{V_i^2} q_w dA = 0 \qquad (30)$$

after applying the Gauss-divergence theorem to the second term and considering that porosity has only spatial variation, we get

$$\int_{V_i^2} \phi \frac{\partial S_w}{\partial \tau} dA - \int_{\Gamma_{V_i^2}} (\lambda_w \nabla \Phi_w) \cdot \mathbf{n} d\Gamma - \int_{V_i^2} q_w dA = 0, \qquad (31)$$

where $\Gamma_{V_i^2}$ is the boundary of the 2-D CV cell around node i.

[44] As stated in section 2.2, matrix and fracture saturations are related through equation (22). Therefore the approximation of the first term of equation (31) gives

$$\int_{V_i^2} \phi \frac{\partial S_w}{\partial \tau} dA \approx A_{\phi i} \frac{\partial S_w^m}{\partial \tau}, \qquad (32)$$

where

$$A_{\phi i} = \sum_{j \in \mathcal{N}_i} \left[\sum_{t \in \mathcal{T}_{ij}} \frac{A_t}{6} \phi_t^m + \sum_{\overline{ij} \in \Omega_f} \frac{dS_w^f}{dS_w^m} \varepsilon_{ij} \frac{|\overline{ij}|}{2} \phi_{\overline{ij}}^f \right], \qquad (33)$$

where A_t is the area of triangle t; ε_{ij} and $|\overline{ij}|$ are the thickness and the measure of the fracture edge $\overline{ij} \in \Omega_f$; and $\phi_{\overline{ij}}^f$ and ϕ_t^m denote the porosity of the fracture and matrix elements, respectively. The first and second terms inside the brackets represent the matrix and fracture pore volumes, respectively, the latter being multiplied by dS_w^f / dS_w^m in order to express the integral in terms of the matrix water saturation.

[45] The second integral term in equation (31) can be approximated by

$$\int_{\Gamma_{V_i^2}} (\lambda_w \nabla \Phi_w) \cdot \mathbf{n} d\Gamma \approx \sum_{j \in \mathcal{N}_i} \left[\sum_{t \in \mathcal{T}_{ij}} |e_{jt}| \left[\lambda_w^m \left(S_w^{m,up} \right) \nabla \Phi_w \right]_{jt} \cdot \mathbf{n}_{jt} \right.$$
$$\left. + \sum_{\overline{ij} \in \Omega_f} \varepsilon_{ij} \lambda_w^f \left(S_w^{f,up} \right) \frac{\partial \Phi_w^f}{\partial \xi} \right], \qquad (34)$$

where superscript *up* denotes an upwinded saturation; $|e_{jt}|$ represents the measure of $\Gamma_{V_i} \cap \Gamma_{V_j}$ inside triangle t and $\mathbf{n}_{jt}$ is the outward normal to this interface; and $\nabla \Phi_w$ is the wetting phase flow potential gradient evaluated at $|e_{jt}|$, which is approximated by equation (29). The term $\partial \Phi_w^f / \partial \xi$ represents the wetting phase flow potential gradient inside the fracture-edge $\overline{ij} \in \Omega_f$. Since the flow in the fracture is considered one-dimensional, this gradient is approximated by

$$\frac{d\Phi_w^f}{d\xi} = \frac{\Phi_j - \Phi_i}{|\overline{ij}|}. \qquad (35)$$

[46] Therefore the first and second terms inside the brackets of equation (34) represent the flux through the 2-D/CV cell boundary and the flux through each fracture (if any) contained in the CV cell.

[47] The third integral term in equation (31) is approximated by

$$\int_{V_i^2} q_w dA \approx q_{wi} A_{V_i^2} = \sum_{j \in \mathcal{N}_i} \left[q_{wi}^m \sum_{t \in \mathcal{T}_{ij}} \frac{A_t}{6} + \sum_{\overline{ij} \in \Omega_f} \varepsilon_{ij} \frac{|\overline{ij}|}{2} q_{w,\overline{ij}}^f \right], \quad (36)$$

where $A_{V_i^2}$ denotes the area of the 2-D/CV cell i.

[48] We can now approximate equation (31) for each control volume i by

$$A_{\phi i} \frac{\partial S_{wi}}{\partial \tau} - \sum_{j \in \mathcal{N}_i} \left[\sum_{t \in \mathcal{T}_{ij}} |e_{jt}| \left[\lambda_w^m \left(S_w^{m,up} \right) \nabla \Phi_w \right]_{jt} \cdot \mathbf{n}_{jt} \right.$$
$$\left. + \sum_{\overline{ij} \in \Omega_f} \lambda_w^f \left(S_w^{f,up} \right) \frac{\partial \Phi_w^f}{\partial \xi} \varepsilon_{ij} \right] - q_{wi} A_{V_i^2} = 0. \qquad (37)$$

[49] A first-order upwind scheme in the saturation is necessary to avoid nonphysical solutions. For the matrix domain, we used the following criteria, referring to the control volume i, having a boundary edge e_{jt} inside the triangle $t \in \mathcal{T}_{ij}$:

$$S_w^{m,up} = \begin{cases} S_{w_i}^m & \text{if } (-\nabla \Phi_w \cdot \mathbf{n})_{jt} > 0 \\ S_{w_j}^m & \text{otherwise} \end{cases} \qquad (38)$$

and for the 1-D fracture domain we used the following criteria:

$$S_w^{f,up} = \begin{cases} S_{w_i}^f & \text{if } \Phi_{w_i} > \Phi_{w_j} \\ S_{w_j}^f & \text{otherwise.} \end{cases} \qquad (39)$$

[50] As can be seen, the upwind criteria in the matrix and fracture domain have a clear physical interpretation; they are based on the flow direction at the interface between two CV cells. In the next section we will compare the CV and the FU-FEM upwind criteria.

[51] The same procedure outlined above can be used for the flow potential equation (equation (8)). Since it has been assumed that flow potentials are the same at the matrix-fracture interface as in the corresponding cells, we have dropped the superscript for this variable. For the 2-D matrix/1-D fracture flow, we get

$$- \sum_{j \in \mathcal{N}_i} \left[\sum_{t \in \mathcal{T}_j} |e_{jt}| \left[\lambda^m \nabla \Phi_w + \lambda_n^m \nabla \Phi_c \right]_{jt} \cdot \mathbf{n}_{jt} \right.$$
$$\left. + \sum_{\overline{ij} \in \Omega_f} \left[\lambda^f \frac{\partial \Phi_w}{\partial \xi} + \lambda_n^f \frac{\partial \Phi_c}{\partial \xi} \right] \varepsilon_{\overline{ij}} \right] - (q_{wi} + q_{ni}) A_{V_i^2} = 0, \qquad (40)$$

where $\lambda = \lambda_w + \lambda_n$ denotes the total mobility.

[52] All mobilities in equation (40) are also upwinded with the criteria established in equations (38) and (39) for 2-D matrix and 1-D fracture elements, respectively. The capillary potential gradient in the fracture is approximated by

$$\frac{\partial \Phi_c^f}{\partial \xi} = \frac{\Phi_{cj} - \Phi_{ci}}{|\overline{ij}|} \qquad (41)$$

[53] The method can be readily extended to the 3-D matrix/2-D fracture formulation. The variable and gradient approximations in the 2-D fracture triangular elements are performed in transformed coordinates. The procedure for the coordinate transformation is given by *Juanes et al.* [2002].

3.4. Comparison of Upwind Criteria

[54] If we use the C-FEM to discretize the saturation equation (equation (9)), the discretization of the second term would lead to a stiffness matrix $\mathbb{K}$. In local coordinates for a triangle B, the matrix is defined by

$$\mathbb{K}_{ij}^B = \int_{\Omega_B} \frac{k_{rw}}{\mu_w} \nabla N_i k \nabla N_j d\Omega_B \quad \text{for } i, j = 1, 2, 3, \qquad (42)$$

where k, k_{rw}, and μ_w are evaluated inside triangle B.

[55] The FU-FEM of *Dalen* [1979] is a modification of the C-FEM method, where the above matrix is distorted to a nodal flow balance:

$$\tilde{\mathbb{K}}_{ij}^B = \begin{cases} k_{rw,ij}^{up} \int_{\Omega_B} \mu_w^{-1} \nabla N_i k \nabla N_j d\Omega_B & \text{if } i \neq j \\ -\sum_{j \neq i} \tilde{\mathbb{K}}_{ij}^B & \text{if } i = j, \end{cases} \qquad (43)$$

where $k_{rw,ij}^{up}$ is the upwinded wetting phase relative permeability at edge $\overline{ij}$.

[56] The integral term in the off-diagonal elements of $\tilde{K}_{ij}^B$ (equation (43)) represents a single-phase flow transmissibility between nodes i, j inside the triangle B.

[57] *Letniowski and Forsyth* [1991] defined γ_{ij} as the total single-phase transmissibility between nodes i and j. In our edge-based notation, γ_{ij} can be expressed as

$$\gamma_{ij} = \sum_{t \in \mathcal{T}_{ij}} \int_{\Omega_t} \mu_w^{-1} \nabla N_i k \nabla N_j d\Omega_t \qquad (44)$$

[58] In the works of *Letniowski and Forsyth* [1991] and *Verma* [1996], the wetting phase flow rate, $Q_{w,ij}$, through nodes i, j is expressed by

$$Q_{w,ij} = k_{rw,ij}^{up} \gamma_{ij} (\Phi_{wi} - \Phi_{wj}) \qquad (45)$$

[59] In the work of *Dalen* [1979] for the FU-FEM, $k_{rw,ij}^{up}$ is upwinded according to the criterion

$$k_{rw,ij}^{up} = \begin{cases} k_{rw,i} & \text{if } (\Phi_{wi} - \Phi_{wj}) > 0 \\ k_{rw,j} & \text{otherwise.} \end{cases} \qquad (46)$$

[60] As can be seen in equation (46), this criterion is based only on the potential difference between nodes i, j. In the 2-D Delaunay meshes, γ_{ij} is always positive, and therefore there is consistency between the sign of the wetting phase potential difference and the direction of the flow rate $Q_{w,ij}$. In the 3-D Delaunay meshes the positivity of γ_{ij} is no longer guaranteed. Thus a wrong upwinding may be performed by using the criteria based only on the wetting phase potential difference. *Forsyth* [1991] pointed out this problem and proposed to use the flow direction in the FU-FEM between nodes as an upwind criterion:

$$k_{rw,ij}^{up} = \begin{cases} k_{rw,i} & \text{if } \gamma_{ij}(\Phi_{wi} - \Phi_{wj}) > 0 \\ k_{rw,j} & \text{otherwise,} \end{cases} \qquad (47)$$

which is inadequate for multiphase flow in 3-D unstructured meshes. For single-phase flow the CV method and the FU-FEM produce the same transmissibility term, γ_{ij} [*Forsyth*, 1990; *Verma*, 1996]. However, for multiphase flow it is not correct to compute the flow rate of the wetting phase from equation (45). If we refer to the 2-D CV cell V_a in Figure 3, we note that there are two boundary segments, $\overline{G_1 M_{ab}}$ and $\overline{M_{ab} G_2}$, associated with the edge $\overline{ab_1}$. The 2-D flow rate between nodes a and b_1 is given by

$$Q_{w,ab_1} = -\int_{G_1}^{M_{ab_1}} \lambda_{w,e_{11}} \nabla \Phi_w^{K_1} \cdot \mathbf{n} d\Gamma - \int_{M_{ab_1}}^{G_2} \lambda_{w,e_{12}} \nabla \Phi_w^{K_2} \cdot \mathbf{n} d\Gamma. \qquad (48)$$

[61] In the CV method the upwinding criterion (equation (38)) based on the flux direction at the interface is applied to each boundary segment. On the other hand, the criterion proposed by *Letniowski and Forsyth* [1991] is based on an averaged single-phase flow direction between nodes a and b_1, attributing the same upwinded property to both boundary segments. Both the FU-FEM and the CV method produce practically the same results in 2-D Delaunay meshes, because this subtle difference is likely to occur in very few nodes and because in the FU-FEM there is a weighted contribution of the flow in each CV

boundary segment. However, in 3-D Delaunay unstructured meshes a tetrahedron edge can be associated with more than 10 boundary surfaces of any given 3-D CV cell. Therefore assigning the same mobility to all the boundary surfaces may lead to unphysical results. This can be verified simply by implementing a numerical method where the flow potential equations are solved by the FU-FEM method and the saturation equation is solved by the CV method. The stability of that implementation would show a strong dependency with the mesh generation in 3-D problems.

[62] In fact, to make the FU-FEM upwind criterion [*Letniowski and Forsyth*, 1991] equivalent to the CV criterion, it would be necessary to have tetrahedra with 3-D CV median dual cells as close as possible to Voronoi cells. Indeed, this is a serious constraint for 3-D unstructured mesh generation, since this would require that each tetrahedron contain its circumsphere inside it. Even in 2-D Delaunay triangulations, it is difficult to obtain Delaunay triangles having their circumcenters inside them, which motivated the use of mixed Voronoi-median cells (also called generalized PEBI cells) in some applications of oil reservoir simulation [*Verma*, 1996; *Verma and Aziz*, 1997].

[63] On the basis of the above analysis, it is clear that unlike the schemes for the FU-FEM, the CV upwinding criterion is consistent with the physics of flow in 2-D and 3-D domains and better suited for 3-D unstructured meshes. We also like to point out that to reduce numerical dispersion, high-order upwinding can be readily implemented in the CV method by increasing the order of approximation of S_w inside the CV cell and using a slope limiter [*Barth and Jespersen*, 1989].

3.5. Edge-Based Code

[64] The integration of equation (34) was performed using an edge-based algorithm. That is, to compute the fluxes through two neighboring CV cells, we swept over all the edges, since the CV boundary segments and normals are associated with each edge of the Delaunay triangulation. Figure 5 shows the algorithm, in pseudocode, for the numerical computation of S_w^{k+1} from equation (37) for the 2-D matrix/1-D fracture flow. The algorithm can be readily extended to the 3-D matrix/2-D fracture flow.

3.6. IMPES Formulation

[65] The IMPES formulation consists of the sequential solution of the decoupled flow potential and saturation equations. All the properties depending on the wetting phase saturation are computed at the previous time level. Equation (40) is solved implicitly in Φ_w:

$$-\sum_{j \in \mathcal{N}_i} \left[\sum_{t \in \mathcal{T}_j} |e_{jt}| (\lambda^{m,k} \nabla \Phi_w^{k+1})_{jt} \cdot \mathbf{n}_{jt} + \sum_{\overline{ij} \in \Omega_f} \varepsilon_{ij} \chi^{f,k} \frac{\partial \Phi_w^{k+1}}{\partial \xi} \right]$$

$$= \sum_{j \in \mathcal{N}_i} \left[\sum_{t \in \mathcal{T}_j} |e_{jt}| (\lambda_n^{m,k} \nabla \Phi_c^k)_{jt} \cdot \mathbf{n}_{jt} + \sum_{\overline{ij} \in \Omega_f} \varepsilon_{ij} \chi_n^{f,k} \frac{\partial \Phi_c^k}{\partial \xi} \right]$$

$$+ (q_{wi} + q_{ni}) A_{V_i^2}, \qquad (49)$$

where superscript k indicates the time-step level.

input   : Φ_w,S_w^k,Mesh geometry
output   : S_w^{k+1}
foreach *node i* **do** $f(i) = 0$;
foreach *triangle K* **do** Compute $\nabla \Phi_W^K$;
foreach *triangle edge l* **do**
    $flux = 0$;
    Determine nodes i and j forming edge l;
    for $t \in \mathcal{T}_j$ **do**
        Extract outward normal to e_{jt};
        Compute upwind mobility in the matrix;
        $flux = flux - |e_{jt}|(\lambda_w^{m,up}\nabla\Phi_w)_{jt} \cdot \mathbf{n}_{jt}$;
    end
    if *edge l is a fracture* **then**
        Compute upwind mobility in the fracture;
        $flux = flux - \epsilon(\lambda_w^{f,up}\dfrac{d\Phi_w^f}{d\xi})$;
    end
    $f(i) = f(i) + flux$;
    $f(j) = f(j) - flux$;
end
foreach *node i* **do**
    $S_w^{k+1}(i) = S_w^k(i) + \dfrac{\Delta t}{V_\phi(i)}(-f(i) + V(i)q_w(i))$;
end

Figure 5. Edge-based algorithm for the numerical computation of S_w^{k+1} in equation (50).

[66] Equation (37) is solved explicitly in S_w with an explicit-Euler integration in time:

$$A_{\phi i}\frac{S_{wi}^{k+1} - S_{wi}^k}{\Delta \tau} = \sum_{j \in \mathcal{N}_i}\left[\sum_{t \in \mathcal{T}_j}|e_{jt}|\left(\lambda_w^{m,k}\nabla\Phi_w^{k+1}\right)_{jt} \cdot \mathbf{n}_{jt}\right.$$
$$\left. + \sum_{\overline{ij} \in \Omega_f}\lambda_w^{f,k}\frac{\partial\Phi_w^{k+1}}{\partial\xi}\right] + q_{wi}A_{V_i^2}. \qquad (50)$$

[67] A simple adaptive time step method was implemented to guarantee stability in time:

[68] 1. Set $\Delta S_{w,min}$, $\Delta S_{w,max}$, and $\beta > 1$.
[69] 2. Determine $x = max(\mathbf{S}_w^{k+1} - \mathbf{S}_w^k)$.
[70] 3. If $x > \Delta S_{w,max}$, then decrease time step: $\Delta t^{k+1} = \Delta t^k/\beta$ and redo the computation.
[71] 4. If $x < \Delta S_{w,min}$, then accept solution and increase time step: $\Delta t^{k+1} = \beta\Delta t^k$.
[72] 5. Otherwise accept the solution and keep the same time step.
[73] In our numerical simulations, we set $\Delta S_{w,min} = 0.005$, $\Delta S_{w,max} = 0.01$, and $\beta = 1.2$.

4. Results

[74] We performed several 2-D and 3-D numerical tests to evaluate the performance of the implemented methods.

Various degrees of nonlinearity in the relative permeability and capillary pressure relationships were considered. We employed the following relations for the relative permeability:
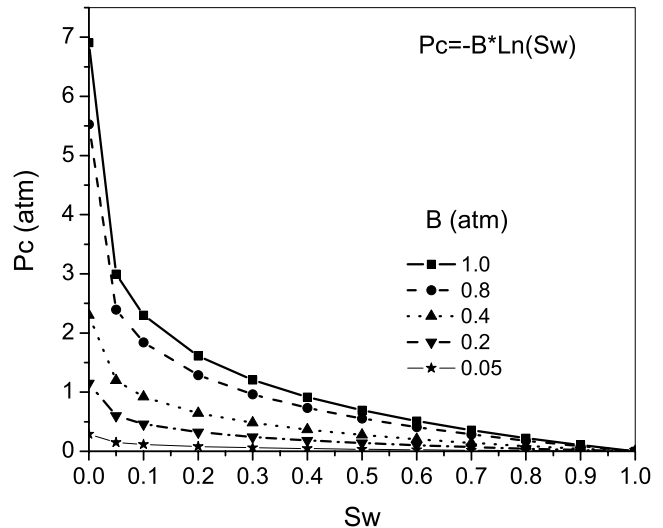
$$k_{rw} = S_w^{\nu_i} \qquad (51)$$

Figure 6. Capillary pressure in the examples.

Table 1. Fluid Properties

Property	Water	Oil
Density, kg/m³	1000	600
Viscosity, Pa-s	0.8×10^{-3}	0.45×10^{-3}

$$k_{rn} = (1 - S_w)^{\nu_i}, \qquad (52)$$

where ν_i ($i = \{m, f\}$) is the matrix or fracture exponent.

[75] For the capillary pressure we used the following relation:

$$P_c = -B_i \ln(S_w), \qquad (53)$$

where B_i ($i = \{m, f\}$) is the matrix or fracture parameter, respectively. This model is suitable for water-wet systems, where water is the wetting phase and oil or NAPL is the nonwetting phase. Figure 6 shows the P_c curves for different values of B_i. Notice that to avoid infinity values at $S_w = 0$, all the capillary pressure curves have been truncated to a finite large value at this point.

[76] When the model of equation (53) is used for the matrix and the fracture, then equation (22) can be written as

$$S_w^f = \left(S_w^m\right)^{B_m/B_f} \qquad (54)$$

and dS_w^f/dS_w^m is given by

$$\frac{dS_w^f}{dS_w^m} = \frac{B_m}{B_f} \left(S_w^m\right)^{B_m/B_f - 1} \qquad (55)$$

[77] In some of our test examples we set $B_m = B_f$, and in some others $B_m \neq B_f$. In some test examples, we neglected capillary pressure ($B_m = B_f = 0$ atm) to show the effect of capillarity.

[78] The 2-D results were compared with a FU-FEM code by *Karimi-Fard and Firoozabadi* [2003], which in turn was validated against a finite difference commercial simulator Eclipse from Schlumberger-Geoquest (2000) with a set of tests that the Eclipse can be used. For the 3-D tests we performed a sensitivity analysis to select the degree of mesh refinement.

[79] Wells were represented as source/sink terms in the control volume containing the well. The flow rates were proportional to the phase mobilities in the control volume containing the production well. The thickness of the fractures in all the examples is 10^{-4} m. The properties of the fluids are shown in Table 1, and those of the rock for both the matrix and the fractures are shown in Table 2. The rock-fluid interactions are spec-
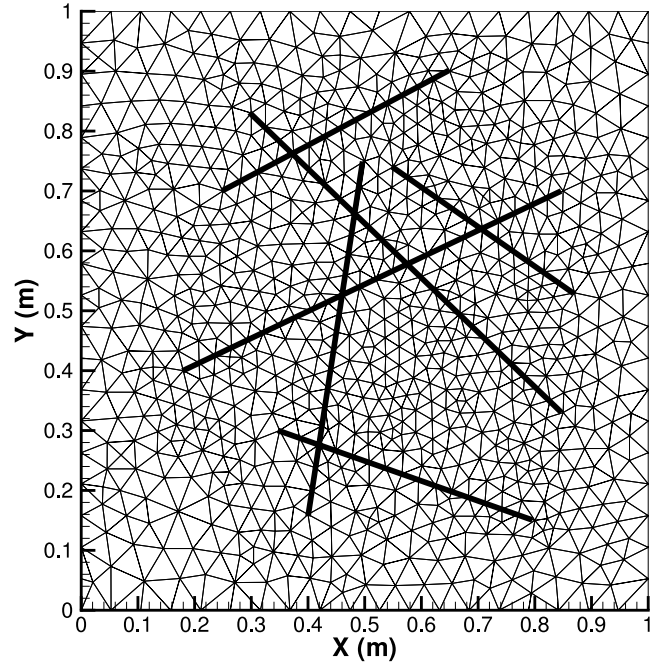
Table 2. Rock Properties

Property	Matrix	Fracture
Porosity, fraction	0.20	1.00
Permeability,[a] m²	9.87×10^{-16}	8.26119×10^{-10}

[a]One millidarcy = 9.87×10^{-16} m².
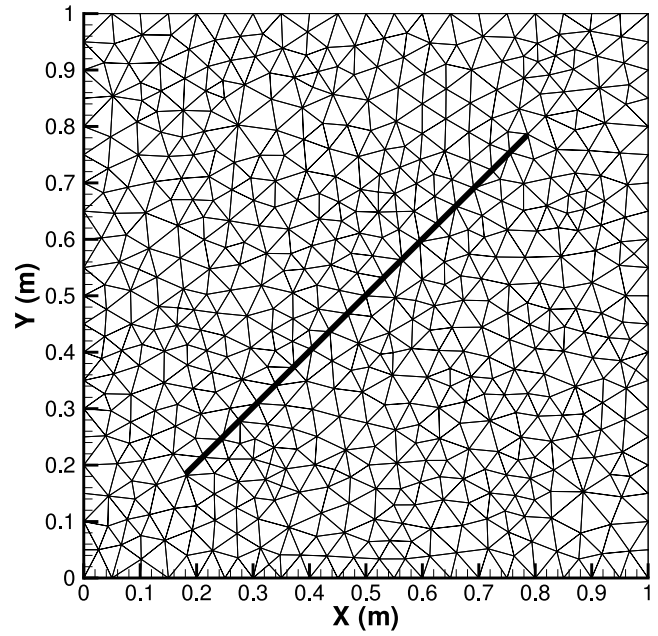
(a)

(b)

Figure 7. Two-dimensional Delaunay conforming mesh for discrete-fractured media: (a) single-fracture configuration and (b) multiple-fracture configuration.

ified for each example by setting parameters B_m and B_f and exponents ν_m and ν_f. All runs were executed on a 2-GHz PC-Pentium 4.

4.1. Two-Dimensional Simulations

[80] In the 2-D examples, water (wetting phase) injection is simulated in a fractured porous medium represented by a

Table 3. Fracture Coordinates (in Meters) for the Multifracture Configuration

Fracture	First Point	Second Point
1	(0.18, 0.40)	(0.75, 0.70)
2	(0.30, 0.83)	(0.85, 0.33)
3	(0.55, 0.74)	(0.87, 0.53)
4	(0.50, 0.75)	(0.40, 0.16)
5	(0.25, 0.70)	(0.65, 0.90)
6	(0.35, 0.30)	(0.80, 0.15)

(a)

(b)

horizontal square domain $[0, 1] \times [0, 1]$ m^2. Two configurations were used in the tests:

[81]   1. The first is a single-fracture medium, where the fracture is represented by a line with coordinates (0.2, 0.2) m and (0.8, 0.8) m. In Figure 7a we show the 2-D Delaunay mesh with 580 nodes used for this matrix-fracture configuration.

[82]   2. The second is a multifracture medium containing six fractures represented by lines with coordinates shown in Table 3. In Figure 7b we show the 2-D Delaunay mesh with 900 nodes used for this configuration.

[83]   For all the examples the injection well was placed at the lower left corner and the production well was placed at the upper right corner. The water flow rate was set to 2.3148×10^{-8} m^3/s, which is equivalent to a displacement of 0.01 PV/d.

[84]   Table 4 lists all the tests performed in 2-D. The relative permeability exponent for equations (51) and (52) was varied from 3 to 5 in the matrix and from 2 to 3 in the fracture. Values of B_m and B_f are also shown in Table 4.

[85]   Figures 8 and 9 show water saturation contours at 50% of PV displacement for nonlinear relative permeabilities in the single-fracture configuration. Figure 8a depicts the results from the simulation where capillary pressure effect is neglected ($B_m = B_f = 0$). Comparison with Figure 8b, where $B_m = B_f = 1.0$ atm, shows that capillary pressure has a significant effect. Figure 8c shows difference in contours by increasing the nonlinearity in relative permeability but keeping the same capillary pressure function for both the matrix and the fracture ($B_m = B_f = 1.0$ atm). Figures 9a, 9b, 9c, and 9d
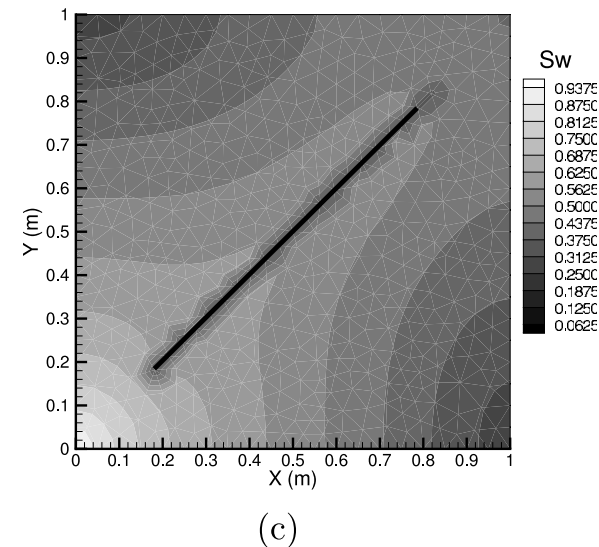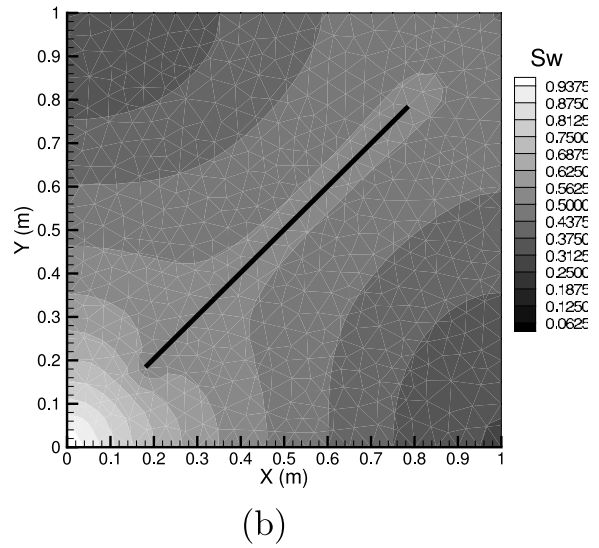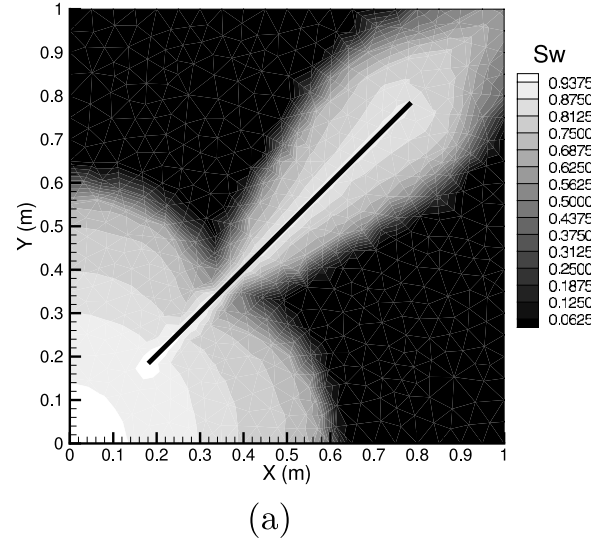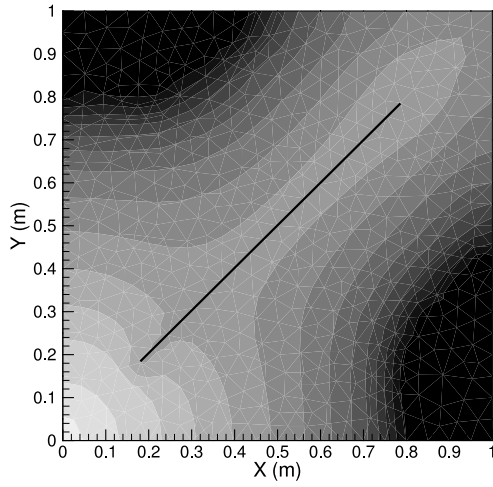
Table 4. Two-Dimensional Conditions and Results

Test ID	B_m, atm	B_f, atm	ν_m	ν_f	Fractures	Displaced PV,[a] %	FU-FEM CPU Time, s	CV CPU Time, s
2D-002-0	0.0	0.0	3	2	1	50	6.64×10^1	8.28×10^1
2D-002-1	1.0	1.0	3	2	1	50	3.41×10^4	4.01×10^4
2D-003-0	1.0	1.0	4	3	1	50	8.43×10^3	1.29×10^4
2D-004-0	1.0	1.0	5	3	1	100	3.33×10^4	4.71×10^4
2D-004-1	1.0	0.8	5	3	1	100	-	4.04×10^4
2D-004-2	1.0	0.2	5	3	1	100	-	6.87×10^3
2D-004-3	1.0	0.05	5	3	1	100	-	4.69×10^3
2D-005-0	1.0	1.0	5	3	6	25	1.33×10^4	1.66×10^4
2D-005-1	1.0	0.2	5	3	6	25	-	1.68×10^2

[a]All tests were performed with an injection rate of 0.01 PV/d.

(c)

Figure 8. Water-saturation contours at 50% PV for nonlinear k_{r_i}: (a) $P_c^m = P_c^f = 0$ and $\nu_m = 3$, $\nu_f = 2$; (b) P_c: $B_m = B_f = 1.0$ atm and $\nu_m = 3$, $\nu_f = 2$; and (c) P_c: $B_m = B_f = 1.0$ atm and $\nu_m = 4$, $\nu_f = 3$.
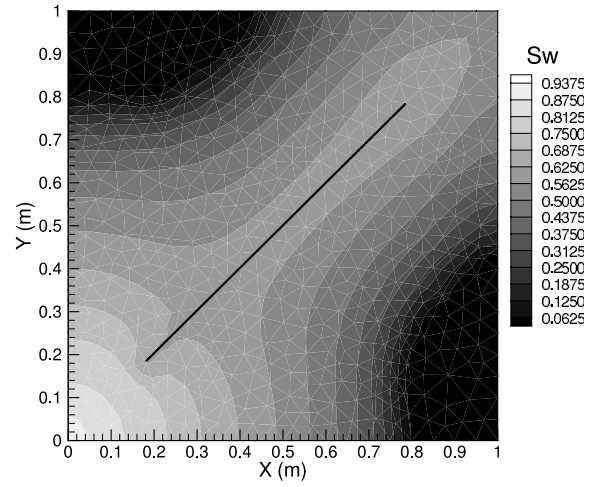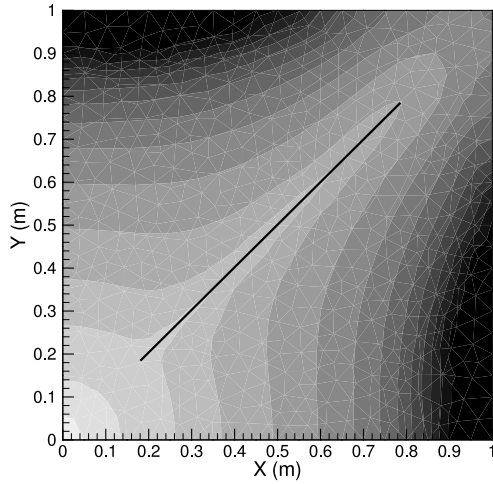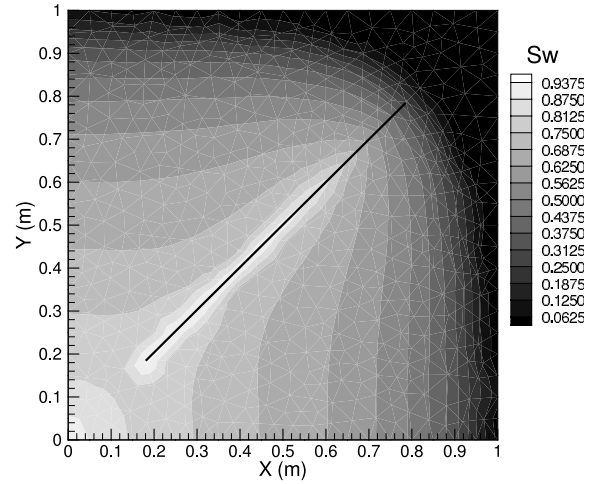
(a)

(b)

(c)

(d)

Figure 9. Water-saturation contours at 50% PV for nonlinear k_{r_i} ($\nu_m = 5$, $\nu_f = 3$): (a) P_c: $B_m = B_f = 1.0$ atm; (b) P_c: $B_m = 1.0$ atm, $B_f = 0.8$ atm; (c) P_c: $B_m = 1.0$ atm, $B_f = 0.2$ atm; (d) P_c: $B_m = 1.0$ atm, $B_f = 0.05$ atm.

show water saturation contours with $\nu_m = 5$, $\nu_f = 3$, $B_m = 1.0$ atm, and by varying B_f from 1.0, 0.8, 0.2, to 0.05 atm, respectively. It can be seen that when the ratio $B_m/B_f = 1.25$, results are similar to that of $B_m/B_f = 1.0$. The saturation results are in agreement with recovery and water-oil ratio plots. The results in Figures 9 and 10 show that when $B_m/B_f = 5.0$ or 20.0, then disparity between matrix and fracture capillary pressure has an influence in flow performance. Results for the multifracture configuration are shown in Figures 11a and

11b, where six fractures have been considered with $\nu_m = 5$, $\nu_f = 3$, and $B_m = 1.0$ atm, and B_f has been varied from 1.0 atm to 0.2 atm, respectively. Again, flow performance is affected by increasing the ratio B_m/B_f. The results for high B_m/B_f are in line with the work of *Terez and Firoozabadi* [1999].

[86] All the 2-D results were practically identical to the 2-D FU-FEM code previously developed by *Karimi-Fard and Firoozabadi* [2003]. CPU performance of both methods is also of the same order of magnitude (see the
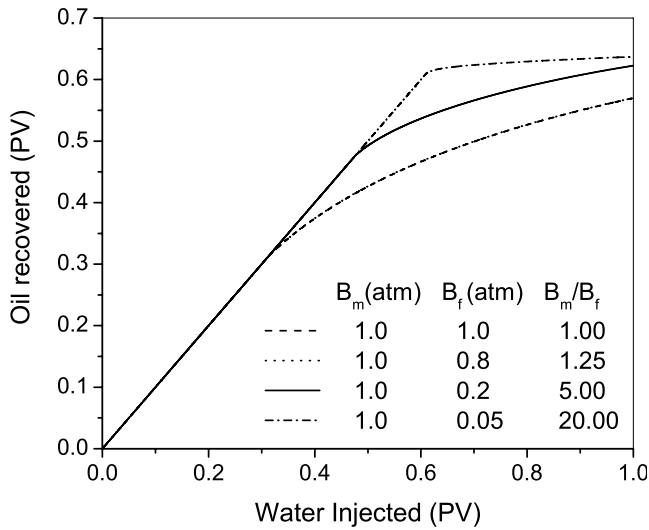
(a)
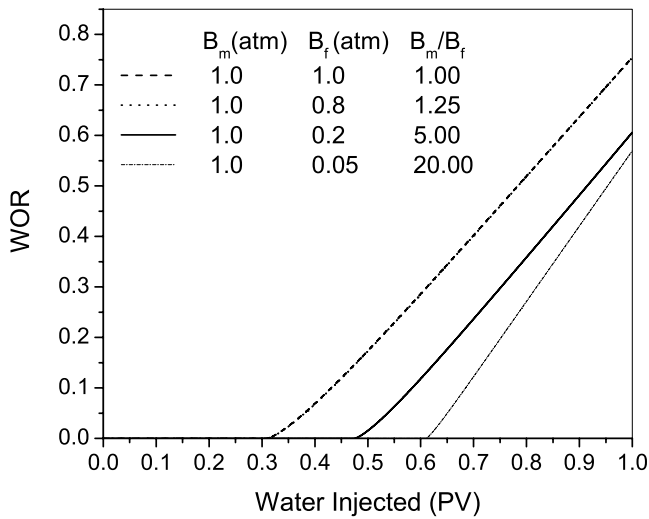
(b)

Figure 10. Effect of ratio B_m/B_f on the 2-D simulation with a single fracture and nonlinear k_{r_i} ($\nu_m = 5$, $\nu_f = 3$): (a) oil recovery curves and (b) water-oil ratio curves.

two right columns of Table 4); the CV requires, on average, 30% more CPU time due to the extra computation of the flow-potential gradient.
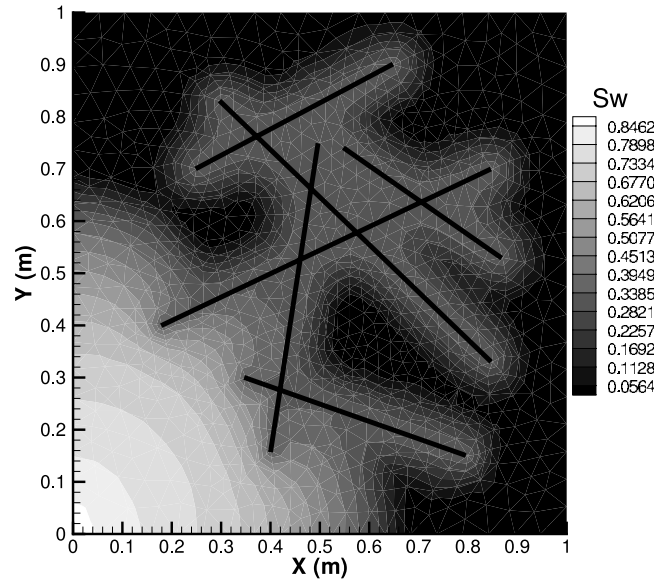
4.2. Three-Dimensional Simulations

[87] Water (wetting phase) injection in a cube of side 20 m was studied to evaluate 3-D implementation of the method. The fractures are represented by parallelograms. Two fracture configurations were tested: (1) 3D-001 and 3D-003, one plane fracture A (see Table 5 and Figure 12a), and (2) 3D-002 and 3D-004, two crossing fractures A, B (see Table 5 and Figure 12b).

[88] Coordinates of parallelograms A and B are shown in Table 5. The Delaunay tetrahedrizations for both

examples are shown in Figure 12. The two examples were gridded with 1100-node meshes. Figure 13 shows a sensitivity study for the two-fracture configuration, 3D-004, that justifies the selected mesh refinement.

[89] In all the examples, the injection and production wells were placed at coordinates (0, 0, 0) and (20, 20, 20) m, respectively. Tests were performed with water

(a)
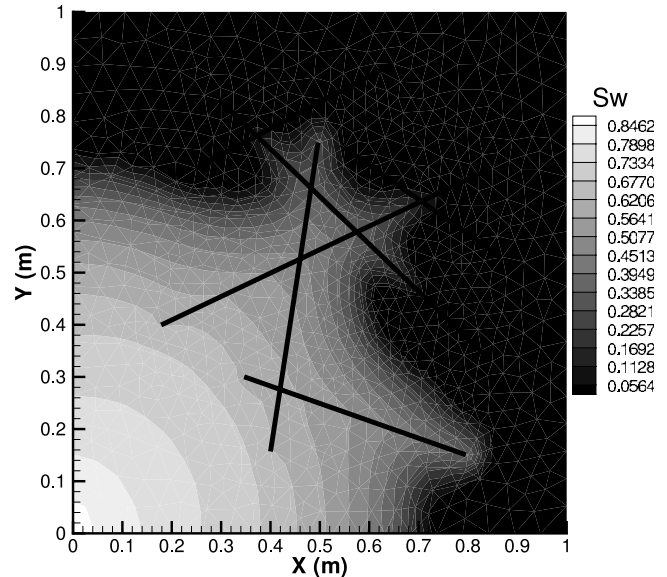
(b)

Figure 11. Water-saturation contours at 25% PV for the multifracture 2-D medium with nonlinear k_{r_i} ($\nu_m = 5$, $\nu_f = 3$): (a) P_c: $B_m = B_f = 1.0$ atm; (b) P_c: $B_m = 1.0$ atm, $B_f = 0.2$ atm.
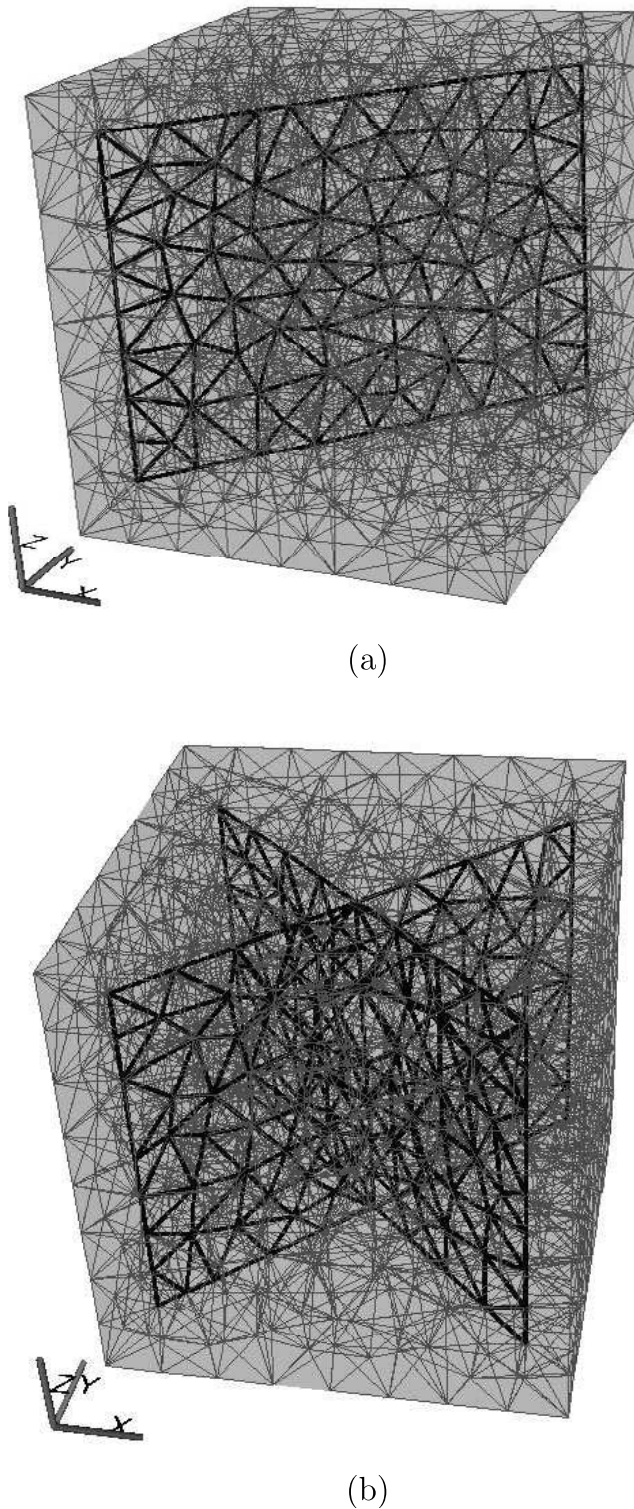
(a)

(b)

Figure 12. Three-dimensional Delaunay conforming mesh for discrete-fractured media: (a) single-fracture configuration and (b) two-fracture configuration.

injection rates of 3.70×10^{-5} m³/s and 3.70×10^{-4} m³/s, equivalent to a displacement of 0.002 and 0.02 PV/d, respectively. Gravity and capillary pressure were taken into account. Some tests were performed without capillary

Table 5. Vertex Coordinates (in Meters) of Fractures for the 3-D Examples

Fracture	Vertex 1	Vertex 2	Vertex 3	Vertex 4
A	(2, 2, 2)	(18, 18, 2)	(18, 18, 18)	(2, 2, 18)
B	(2, 18, 2)	(18, 2, 2)	(18, 2, 18)	(2, 18, 18)

pressure to compare simulation results. Table 6 shows the specifications for each test and the performance of the runs.

[90] Figures 14 and 15 show water saturation contours at 20% PV displacement for the single-fracture and two-fracture configurations, and with and without capillary pressure. Notice that the flow pattern through the matrix is shown as a projection into the planes XY, XZ, and YZ. Figures 16 and 17 show the difference in oil recovery and water-oil ratio (WOR) due to capillary pressure for the single-fracture and two-fracture configurations, respectively. Notice that capillary pressure improves the sweep and therefore the performance.

[91] Figure 18 shows results for nonlinear relative permeabilities for the single- and the two-fracture configurations at 20% PV displacement. The second fracture plane improves the performance of water injection.

5. Concluding Remarks

[92] We have presented a physically coherent mathematical formulation for two-phase flow in fractured media using the discrete-fracture model employing the capillary pressure and flux continuity concepts at the matrix-fracture interface. The unique characteristic of the model is that there is no need to compute matrix-fracture exchange flux.

[93] To the best of our knowledge, this is the first time that the 3-D simulation of two-phase flow in fractured porous media with gravity and highly nonlinear capillary pressure and relative permeability using the discrete-
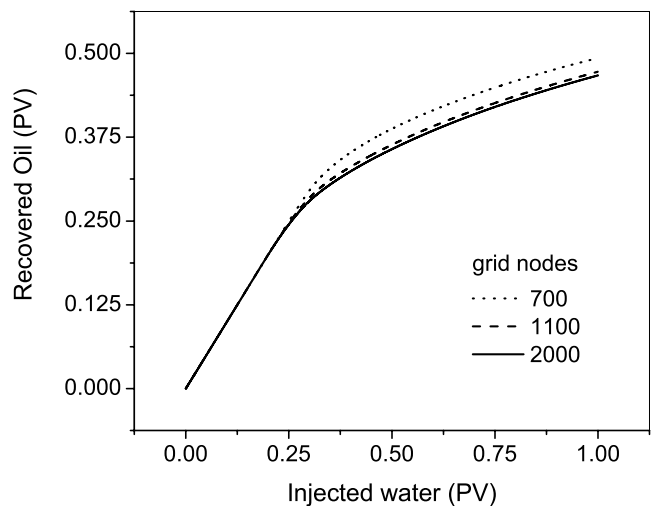

Figure 13. Sensitivity analysis of the 3-D CV method: two-fracture configuration, nonlinear k_{ri} ($\nu_m = 5$, $\nu_f = 3$), and P_c: $B_m = B_f = 0.4$ atm.

Table 6. Three-Dimensional Conditions and Results

Test ID	B_m, atm	B_f, atm	ν_m	ν_f	Fractures	Injection Rate, PV/d	CV CPU Time,[a] s
3D-001-0	0.0	0.0	1	1	1	0.002	3.20×10^2
3D-001-1	0.4	0.4	1	1	1	0.002	2.82×10^2
3D-002-0	0.0	0.0	1	1	2	0.002	4.15×10^2
3D-002-1	0.4	0.4	1	1	2	0.002	3.85×10^2
3D-003-0	1.0	1.0	5	3	1	0.02	4.62×10^2
3D-004-0	1.0	1.0	5	3	2	0.02	1.10×10^3

[a]All runs for 100% of PV displacement.

fracture model is successfully carried out. Although our numerical tests are for impervious boundaries, there is no restriction on the boundary conditions. Indeed we have applied the model to a large-scale problem to predict oil recovery from a fractured reservoir with Dirichlet boundary conditions in the matrix and fractures and placing a horizontal well in a fault. Results of this simulation will be presented in a future publication.

[94] The FU-FEM of *Dalen* [1979] is applicable only to the 2-D Delaunay triangulations because its upwind criterion is based on nodal potential difference and not the flow direction. *Forsyth* [1991] proposed an improved upwind criterion, but the 3-D mesh generation proposed in the work of *Letniowski and Forsyth* [1991] is inadequate for the kind of mesh required in the discrete-fracture model. On the other hand, the control volume method, with a first-order upwind scheme, has a clear physical meaning based on the analysis of the flow direction at the boundary of each control volume. In addition, all the concepts from the finite volume method, such as high-order upwinding and numerical fluxes, can be incorporated readily into the model.

[95] Capillary pressure must be considered when simulating two-phase immiscible flow in fractured media. Flow pattern and recovery predictions may change substantially when this property is disregarded.

[96] Difference in capillary pressure functions between matrix and fracture may alter the flow pattern and thus recovery prediction.

Appendix A: Detailed Derivation of the Matrix-Fracture Flow Equations

[97] For a matrix and fracture grid next to each other, one can write the following conditions:

[98] 1. From the cross-equilibrium concept, the pressure of each phase is the same in the matrix and fracture nodes next to each other, leading to equality in the flow potentials:

$$\Phi_i^m = \Phi_i^f, \text{where i} = \{w, n\}. \tag{A1}$$

[99] 2. There exists a corresponding relationship between capillary pressures:

$$P_c^m(S_w^m) = P_c^f(S_w^f). \tag{A2}$$

[100] 3. The fluxes at the matrix-fracture interfaces are equal:

$$\hat{q}_i^m = \hat{q}_i^f, \text{where i} = \{w, n\}. \tag{A3}$$

[101] The flow equations for two phase flow in porous media (equations (8) and (9)) when applied to both matrix and fractures and discretized in space, transform into a set of differential-algebraic equations (DAE):

$$\mathbf{K}_t^m \mathbf{\Phi}_w^m + \mathbf{K}_n^m \mathbf{\Phi}_c^m + \mathbf{M}^m(\mathbf{q}_w^m + \mathbf{q}_n^m) + \mathbf{Q}_w^m + \mathbf{Q}_n^m = \mathbf{0} \tag{A4}$$

$$\mathbf{M}_\phi^m \frac{d}{dt}\mathbf{S}_w^m + \mathbf{K}_w^m \mathbf{\Phi}_w^m + \mathbf{M}^m \mathbf{q}_w^m + \mathbf{Q}_w^m = \mathbf{0} \tag{A5}$$
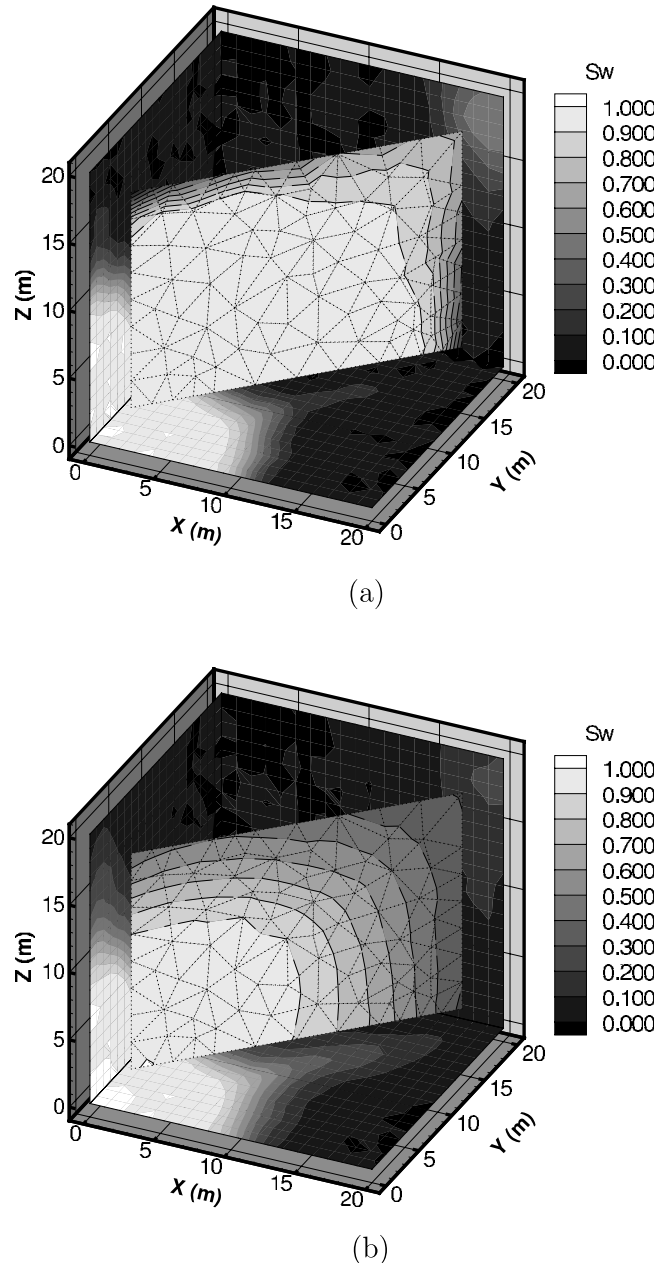

(a)

(b)

Figure 14. Water-saturation contours at 20% PV for 3-D tests with the single-fracture configuration, linear k_r, and rate = 0.002 PV/d: (a) $P_c = 0$ and (b) P_c: $B_m = Bf = 0.4$ atm.
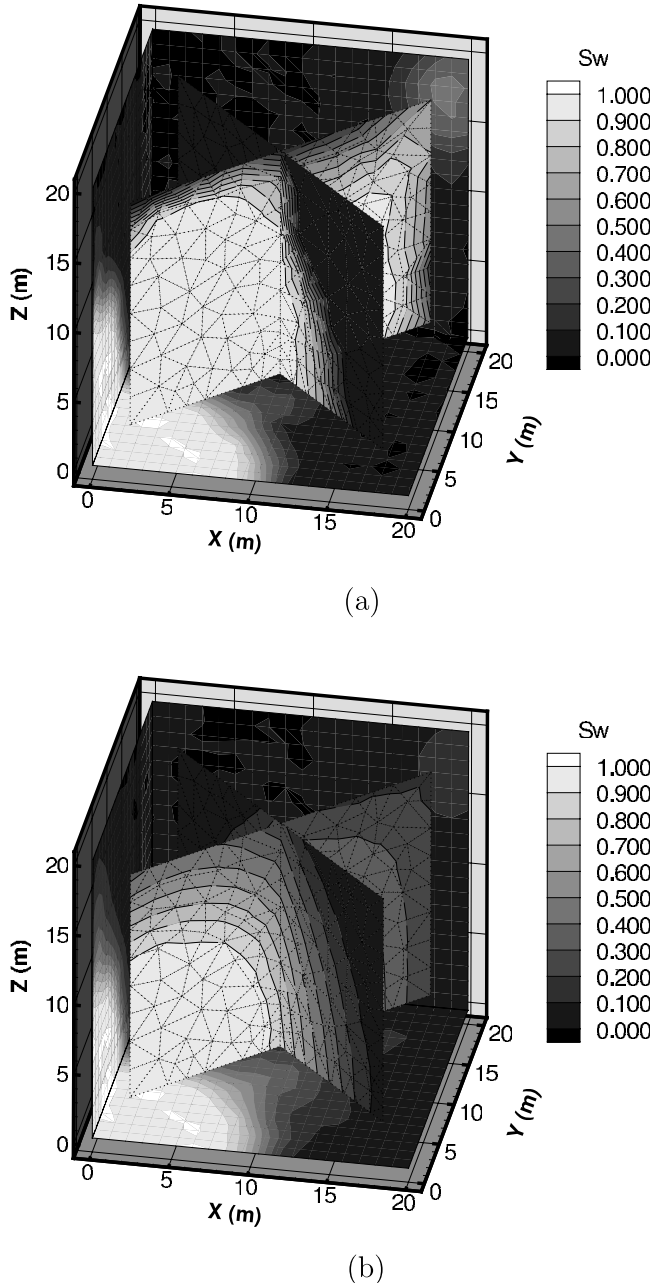
(a)

(b)

Figure 15. Water-saturation contours at 20% PV for 3-D tests with the two-fracture configuration, linear k_{r_i}, and rate = 0.002 PV/d: (a) $P_c = 0$ and (b) P_c: $B_m = B_f = 0.4$ atm.

for the matrix and

$$\mathbf{K}_t^f \boldsymbol{\Phi}_w^f + \mathbf{K}_n^f \boldsymbol{\Phi}_c^f + \mathbf{M}^f \left(\mathbf{q}_w^f + \mathbf{q}_n^f \right) + \mathbf{Q}_w^f + \mathbf{Q}_n^f = \mathbf{0} \qquad (A6)$$

$$\mathbf{M}_\phi^f \frac{d}{dt} \mathbf{S}_w^f + \mathbf{K}_w^f \mathbf{F}_w^m + \mathbf{M}^f \mathbf{q}_w^f + \mathbf{Q}_w^f = \mathbf{0} \qquad (A7)$$

for the fractures. In equations (A4)–(A7), superscripts m and f denote properties and variables in the matrix and the fracture, respectively; $\boldsymbol{\Phi}_w$, $\mathbf{S}_w$, and $\boldsymbol{\Phi}_c$ are vectors containing the water flow potential, water saturation, and

capillary potential, respectively, at the matrix and fracture nodes; $\mathbf{K}_i$ for $i = w$, n, t are the stiffness matrices formed with mobilities λ_w, λ_n, and $\lambda_t = \lambda_w + \lambda_n$, respectively; $\mathbf{M}$ is a diagonal matrix containing the area (in 2-D) or the volume (in 3-D) of the matrix and fracture entities inside the CV cell; $\mathbf{M}_\phi$ is a diagonal mass matrix containing the corresponding pore volume of the matrix or fracture entities inside the CV cell. Time derivatives may be approximated with a forward Euler, for example. Vectors $\mathbf{q}_i^m$ and $\mathbf{q}_i^f$ contain source/sink terms inside each CV cell. Vectors $\mathbf{Q}_i^m$ and $\mathbf{Q}_i^f$ for $i = n$, w contain the flow transfer terms between the matrix and fracture inside each CV
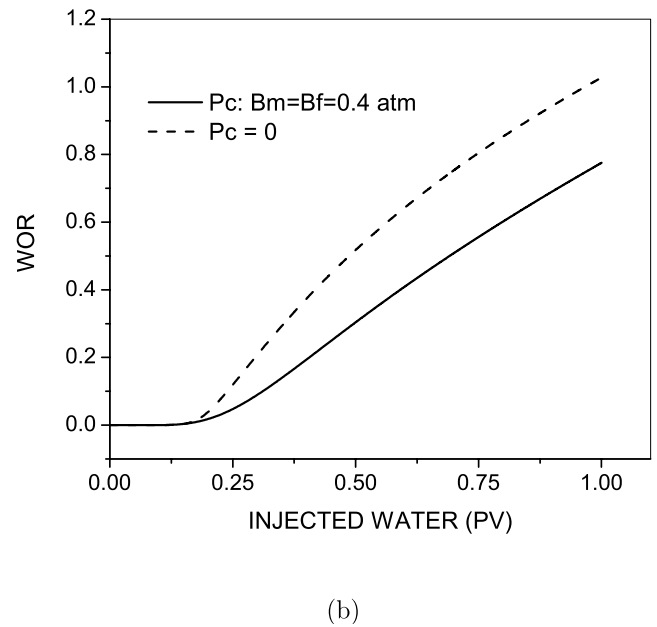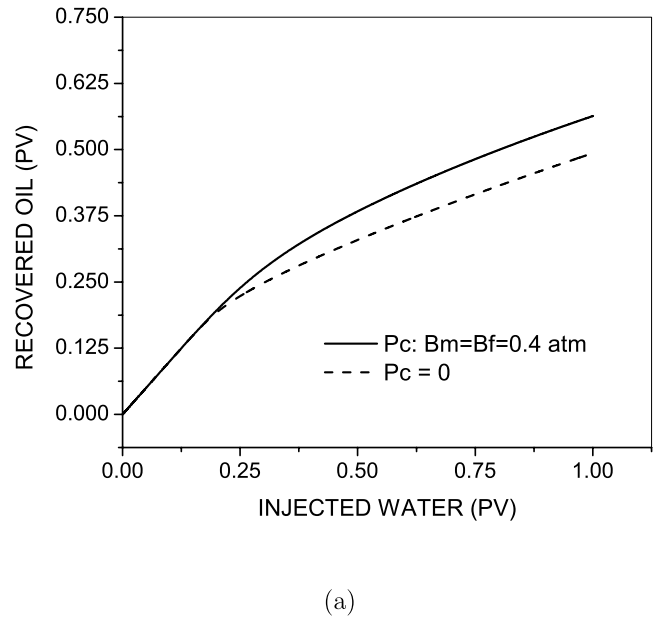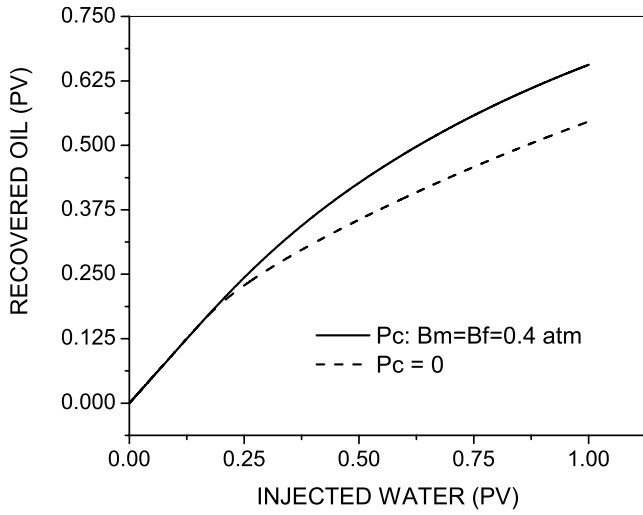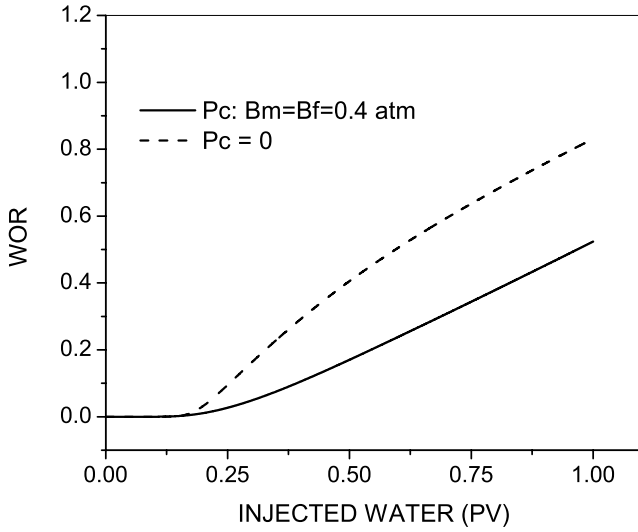

(a)

(b)

Figure 16. Three-dimensional simulations for the single-fracture configuration with linear k_{r_i} and rate = 0.002 PV: (a) recovery and (b) water-oil ratio at production well.

(a)

(b)

Figure 17. Three-dimensional simulations for the two-fracture configuration with linear k_{r_i} and rate = 0.002 PV: (a) recovery and (b) water-oil ratio at production well.

Equations (A4)–(A7) should be solved in the variables Φ_w^m, Φ_w^f, S_w^m, and S_w^f. However, in our formulation we reduce the number of variables by employing conditions 1−3 stated above. Flow potential equality allows addition of equations (A4) and (A6). Capillary pressure equality establishes a relation between matrix and fracture node saturations:

$$S_w^f = \left[P_c^f \right]^{-1} P_c^m \left(S_w^m \right). \tag{A8}$$
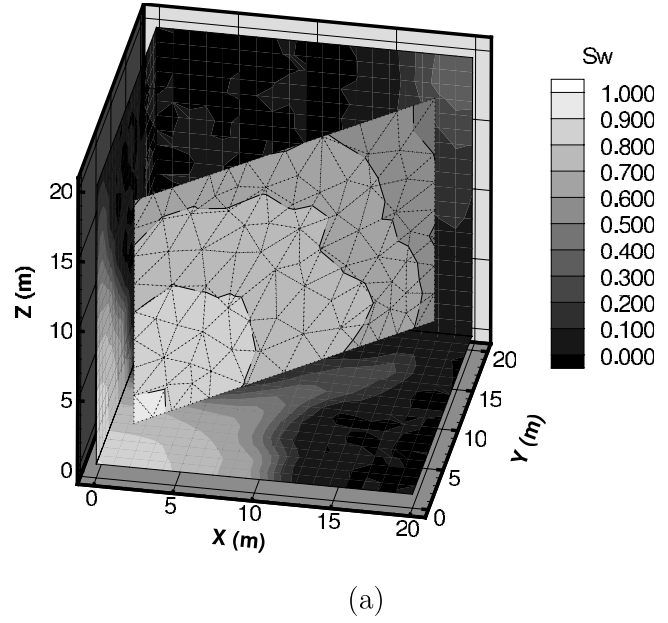
(a)

(b)

Figure 18. Water-saturation contours at 20% PV for the 3-D tests with nonlinear k_{r_i} ($\nu_m = 5$, $\nu_f = 3$) and P_c: $B_m = B_f =$ 1.0 atm: (a) single-fracture configuration and (b) two-fracture configuration.
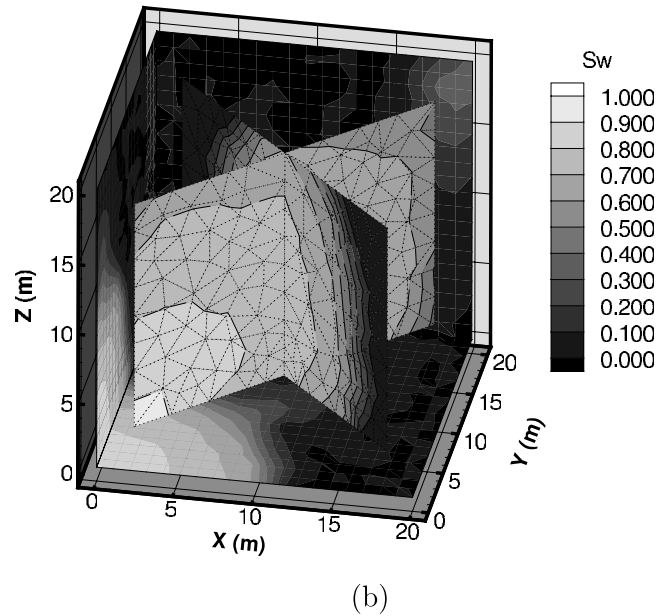
cell containing a fracture; otherwise the entry is zero. Since condition 3 establishes the equality of fluxes across the matrix-fracture interface, then $\mathbf{Q}_i^m + \mathbf{Q}_i^f = \mathbf{0}$, and therefore there is no need to compute transfer terms in our formulation since matrix and fracture flow equations will be added inside each CV cell. The entries of all the matrices depend on the properties of the media: fluid, rock, and rock-fluid properties of the matrix and fracture, and the geometry of the mesh entities representing the matrix and fractures. We represent fractures as (*n*-1) dimensional entities, but the corresponding domain dimensionality is recovered by multipling all entries of $\mathbf{M}^f$, $\mathbf{M}_\phi^f$, and $\mathbf{K}_i^f$ by the corresponding fracture thickness.

For example, if we use the model $P_c = -B ln(S_w)$ for both the matrix and the fracture, then

$$S_w^f = \left(S_w^m\right)^{B_m/B_f}. \tag{A9}$$

Therefore equation (A8) is used to express time derivatives in equation (A7) in terms of S_w^m by using the chain rule:

$$\frac{dS_w^f}{dt} = \frac{dS_w^f}{dS_w^m}\frac{dS_w^m}{dt}. \tag{A10}$$

For example, for the model in equation (A9), dS_w^f/dS_w^m is given by

$$\frac{dS_w^f}{dS_w^m} = \frac{B_m}{B_f}\left(S_w^m\right)^{B_m/B_f - 1}. \tag{A11}$$

As can be seen in equation (A10), dS_w^f/dt is equal to dS_w^m/dt only if $dS_{wi}^f/dS_{wi}^m = 1$, i.e., when the matrix and fracture capillary curves are the same. Equation (A8) maps S_w^f into S_w^m, and therefore one can compute all the rock-fluid properties in the fracture from S_w^m. In equation (23), $\lambda_w^f = \lambda_w^f(S_w^f)$ or $\lambda_w^f = \lambda_w^f(S_w^f(S_w^m))$. The same applies to λ_n^f; then the matrices $\mathbf{K}_i^f$ in equations (A6) and (A7) are computed with S_w^m. The system of DAE equations (A4)–(A7) reduces to

$$\left(\mathbf{K}_t^m + \mathbf{K}_t^f\right)\boldsymbol{\Phi}_w^m + \left(\mathbf{K}_n^m + \mathbf{K}_n^f\right)\boldsymbol{\Phi}_c^m$$
$$+ \mathbf{M}^m\left(\mathbf{q}_w^m + \mathbf{q}_n^m\right) + \mathbf{M}^f\left(\mathbf{q}_w^f + \mathbf{q}_n^f\right) = 0 \tag{A12}$$

$$\left(\mathbf{M}_\phi^m + \mathbf{M}_\phi^f \mathbf{Z}\right)\frac{d}{dt}\mathbf{S}_w^m + \left(\mathbf{K}_w^m + \mathbf{K}_w^f\right)\boldsymbol{\Phi}_w^m + \mathbf{M}^m\mathbf{q}_w^m + \mathbf{M}^f\mathbf{q}_w^f = 0, \tag{A13}$$

where $\mathbf{Z}$ is a diagonal matrix with entries $\mathbf{Z}_{ii} = dS_{wi}^f/dS_{wi}^m$ if the CV cell i contains a fracture, or zero otherwise.

References

Aziz, K., and A. Settari (1979), *Petroleum Reservoir Simulation*, Appl. Sci., London.

Baca, R., R. Arnett, and D. Langford (1984), Modeling fluid flow in fractured porous rock masses by finite element techniques, *Int. J. Numer. Meth. Fluids*, 4, 337–348.

Baliga, B., and S. Patankar (1980), A new finite-element formulation for convection-diffusion problems, *Numer. Heat Transfer*, 3, 393–409.

Barth, T., and D. Jespersen (1989), The design and application of upwind schemes on unstructured meshes, paper AIAA-89-0366 presented at the 27th Aerospace Sciences Meeting, Am. Inst. of Aeronaut. and Astronaut., Reno, Nev.

Bastian, P., R. Helmig, H. Jakobs, and V. Reichenberger (2000), Numerical simulation of multiphase flow in fractured porous media, in *Numerical Treatment of Multiphase Flows in Porous Media*, edited by Z. Chen, R. E. Ewing, and Z.-C. Shi, pp. 1–18, Springer-Verlag, New York.

Brooks, A., and T. Hughes (1982), Streamline upwind/Petrov-Galerkin formulations for convection dominated flows with particular emphasis on the incompressible Navier-Stokes equations, *Comput. Methods Appl. Mech. Eng.*, 32, 199–259.

Dalen, V. (1979), Simplified finite-element models for reservoir flow problems, *SPE J.*, 19, 333–343.

Firoozabadi, A., and J. Hauge (1990), Capillary pressure in fractured porous media, *JPT J. Pet. Technol.*, pp. 784–791, June.

Firoozabadi, A., and K. Ishimoto (1994), Reinfiltration in fractured porous media: 1. One-dimensional model, *SPE Adv. Technol.*, 2(2), 35–44.

Fleischmann, P., R. Kosik, B. Haindl, and S. Selberherr (1999), Simple mesh examples to illustrate specific finite element mesh requirements, in *8th International Meshing Roundtable*, pp. 241–246, Sandia Natl. Lab., South Lake Tahoe, Calif.

Forsyth, P. (1990), A control-volume, finite-element method for local mesh refinement in thermal reservoir simulation, *SPE Reservoir Eng.*, 5, 561–566.

Forsyth, P. (1991), A control volume finite element approach to NAPL groundwater contamination, *SIAM J. Sci. Stat. Comput.*, 12(5), 1029–1057.

Freitag, L. A., and C. Ollivier-Gooch (1996), A comparison of tetrahedral mesh improvement techniques, in *5th International Meshing Roundtable*, pp. 87–106, Sandia Natl. Lab., South Lake Tahoe, Calif.

Geiger, S., S. Roberts, S. Matthai, and C. Zoppou (2003), Combining finite volume and finite element methods to simulate fluid flow in geological media, *ANZIAM J.*, 44(E), C180–C201.

Granet, S., P. Fabrie, P. Lemmonier, and M. Quitard (1998), A single phase flow simulation of fractured reservoir using a discrete representation of fractures, paper C-12 presented at the 6th European Conference on the Mathematics of Oil Recovery (ECMOR VI), Eur. Assoc. of Geosci. and Eng., Peebles, Scotland, UK.

Helmig, R. (1997), *Multiphase Flow and Transport Processes in the Subsurface*, 1st ed., Springer-Verlag, New York.

Helmig, R., and R. Huber (1998), Comparison of Galerkin-type discretization techniques for two-phase flow in heterogeneous porous media, *Adv. Water Resour.*, 21(8), 697–711.

Hughes, T., and M. Mallet (1986), A new finite element formulation for computational fluid dynamics: IV. A discontinuity-capturing operator for multidimensional advective-diffusive systems, *Comp. Methods Appl. Mech. Eng.*, 58, 329–336.

Huyakorn, P., B. Lester, and C. Faust (1983), Finite element techniques for modeling groundwater flow in fractured aquifers, *Water Resour. Res.*, 19(4), 1019–1035.

Juanes, R., J. Samper, and J. Molinero (2002), A general and efficient formulation of fractures and boundary conditions in the finite element method, *Int. J. Numer. Meth. Eng.*, 54, 1751–1774.

Karimi-Fard, M., and A. Firoozabadi (2003), Numerical simulation of water injection in 2D fractured media using discrete-fracture model, *SPE Reservoir Eval. Eng.*, 4, 117–126.

Karimi-Fard, M., L. Durlofsky, and K. Aziz (2003), An efficient discrete fracture model applicable for general purpose reservoir simulators, paper SPE 79699 presented at the SPE Reservoir Simulation Symposium, Soc. Pet. Eng., Houston, Tex.

Kazemi, H. (1969), Pressure transient analysis of naturally fractured reservoirs with uniform fracture distribution, *SPE J.*, 9, 451–462.

Kim, J., and M. Deo (1999), Comparison of the performance of a discrete fracture multiphase model with those using conventional methods, paper SPE 51928 presented at the SPE Reservoir Simulation Symposium, Soc. Pet. Eng., Houston, Tex.

Kim, J., and M. Deo (2000), Finite element, discrete fracture model for multiphase flow in porous media, *AIChE J.*, 46(6), 1120–1130.

Lemmonier, P. (1979), Improvement of reservoir simulation by a triangular discontinuous finite element method, paper SPE 8249 presented at the 54th Annual Fall Technical Conference and Exhibition, Soc. of Pet. Eng., Las Vegas, Nev.

Letniowski, F., and P. Forsyth (1991), A control volume finite element method for three-dimensional NAPL contamination problems, *Int. J. Numer. Meth. Fluids*, 13, 955–970.

Lewis, R., E. Verner, and O. Zienckiewicz (1974), A finite element approach to two-phase flow in porous media, in *International Symposium on Finite Element Methods in Flow Problems*, pp. 535–540, UAH Press, Huntsville, Ala.

Michel, A. (2003), A finite volume scheme for two-phase immiscible flow in porous media, *SIAM J. Numer. Anal.*, 41(4), 1301–1317.

Noorishad, J., and M. Mehran (1982), An upstream finite element method for solution of transient transport equation in fractured porous media, *Water Resour. Res.*, 18(3), 588–596.

Peaceman, D. (1977), *Fundamentals of Numerical Reservoir Simulation*, Elsevier-Sci., New York.

Pritchett, J. (1995), Star: A geothermal reservoir simulation system, in *Proceedings of the World Geothermal Congress*, pp. 2959–2963, Int. Geotherm. Assoc., Florence, Italy.

Pruess, K., C. Oldenburg, and G. Moridis (1999), Tough2 user's guide, version 2.0, *Tech. Rep. LBNL-43134*, Lawrence Berkeley Natl. Lab., Berkeley, Calif.

Rabbani, M. (1994), Direct-formulation finite element (DFFE) method for groundwater flow modeling: Two-dimensional case, *SIAM J. Appl. Math.*, *54*(3), 660–673.

Rabbani, M., and J. Warner (1994), Shortcomings of existing finite element formulations for subsurface water pollution modeling and its rectification: One-dimensional case, *SIAM J. Appl. Math.*, *54*(3), 660–673.

Shewchuk, J. (1996), Triangle: Engineering a 2D quality mesh generator and Delaunay triangulator, in *First Workshop on Applied Computational Geometry*, pp. 124–133, Assoc. for Comput. Mach., Philadelphia, Pa.

Si, H. (2002), Tetgen: A 3D Delaunay tetrahedral mesh generator: V.1.2 users manual, *Tech. Rep. 4*, Weierstrass Inst. for Appl. Anal. and Stochast., Berlin, Germany.

Tan, C., and A. Firoozabadi (1995), Theoretical analysis of miscible displacement in fractured porous media: I. Theory, *J. Can. Petrol. Technol.*, *34*(2), 17–27.

Terez, I., and A. Firoozabadi (1999), Water injection in water-wet fractured porous media: Experiments and a new model using modified Buckley-Leverett theory, *SPE J.*, *4*(2), 134–141.

Thomas, L., T. Dixon, and R. Pierson (1983), Fractured reservoir simulation, *SPE J.*, *23*, 42–54.

van Duijn, C., J. Molenaar, and M. de Neef (1994), The effect of capillary forces on immiscible two-phase flow in heterogeneous porous media, *Tech. Rep. 94-103*, Fac. of Tech. Math. and Informatics, Delft Univ. of Technol., Delft, Netherlands.

Verma, S. (1996), Flexible grids for reservoir simulation, Ph.D. thesis, Dep. of Pet. Eng., Stanford Univ., Stanford, Calif.

Verma, S., and K. Aziz (1997), A control volume scheme for flexible grids in reservoir simulation, paper SPE 37999 presented at the Reservoir Simulation Symposium, Soc. of Pet. Eng., Dallas, Tex.

Warren, J., and P. Root (1963), The behavior of naturally fractured reservoirs, *SPE J.*, *3*, 245–255.

Zienkiewicz, O., and R. Taylor (2000), *The Finite Element Method: I. The Basis*, 5th ed., Butterworth-Heinemann, Woburn, Mass.

Zyvoloski, A., A. Robinson, V. Dash, and L. Trease (1994), User's manual for the FEHMN application, *Tech. Rep. LA-UR-94-3788*, Geoanalysis Group, Los Alamos Natl. Lab., Los Alamos, N. M.

————————————

A. Firoozabadi and J. E. P. Monteagudo, Reservoir Engineering Research Institute, 385 Sherman Avenue, Suite 5, Palo Alto, CA 94306, USA. (af@rerinst.org; jorge@rerinst.org)